UNIVERSIDAD DE GUANAJUATO

Campus León

División de Ciencias e Ingenierías

Novel reconstruction algorithm for photoacoustic imaging: toward the quantitative imaging

Thesis

Submitted for the degree of:

Doctor of Physics

Presents:

M.F. Guadalupe Misael Ruiz Veloz

Adviser:

Prof. Dr. Gerardo Gutiérrez Juárez

León Guanajuato, México. March 2023.

In loving memory of my mother, Ma. del Refugio Veloz Rodríguez, who dedicated her life for me and my brother to study. This achievement was supposed to be a reward of your effort and dedication, now it is dedicated to honor your memory.

ii

The work presented in this thesis led to the publication of the following peer-reviewed articles:

- **Misael Ruiz-Veloz**, Geminiano Martínez-Ponce, Rafael I. Fernández-Ayala, Rigoberto Castro-Beltrán, Luis Polo-Parada, Bartolome Reyes-Ramírez, and **Gerardo Gutiérrez-Juárez** , *"Thermally corrected solutions of the one-dimensional wave equation for the laser-induced ultrasound"*, **Journal of Applied Physics** 130, 025104 (2021) https://doi.org/10.1063/5.0050895

- **Misael Ruiz-Veloz**, **Gerardo Gutiérrez-Juárez**, Luis Polo-Parada, Francisco Cortalezzi, David D. Kline, Heather A. Dantzler, Lorena Cruz-Alvarez, Rigoberto Castro-Beltrán, and Carlos Hidalgo-Valadez , *"Image reconstruction algorithm for laser-induced ultrasonic imaging: The single sensor scanning synthetic aperture focusing technique"*, **The Journal of the Acoustical Society of America** 153, 560-572 (2023) https://doi.org/10.1121/10.0016996

Acknowledgements

I wish to show my appreciation to Dr. Gerardo Gutiérrez-Juárez, professor at the Universidad de Guanajuato. Being my adviser during my doctoral studies is a reason itself to be thankful with him, but I am grateful and indebted to him for his patience and help, beyond academic matters, during hard times that arose in the middle of the doctorate.

I wish to extend my special thanks to Dr. Luis Polo-Parada, professor at the Dalton Cardiovascular Research Center at the University of Missouri, for performing the experiments to obtain the results and analysis presented in the chapter 3 of this thesis. And equally important, for the insightful discussions and proposals during the development of the reconstruction algorithm presented. He played a role as an advisor for me.

I would like to thank to Dr. Geminiano Martínez-Ponce, professor at the Centro de Investigaciones en Óptica, for having facilitated the experimental data used to test and analyze the theoretical proposals presented in the chapter 4 of this thesis.

The assistance provided by Dr. Rigoberto Castro-Beltrán, Dr. Arturo González-Vega, Dr. Carlos Herman Wiechers-Medina, and Dr. José Torres-Arenas, being part of my evaluation committee, and their effort and invested time listening to my progress and giving me feedback, is greatly appreciated.

Finally, I want to thank Osvaldo Emmanuel Ruiz Veloz, my brother, for helping me in the development of the schematic representations presented as figures throughout this thesis.

Contents

Summary

This thesis aims to study the photoacoustic imaging technique, this comprises two aspects: the detection technique, and the image reconstruction methods, both studied in this work along with the proposal of a reconstruction algorithm and a mathematical model of the photoacoustic electrical signal.

The thesis is divided in five chapters:

1. The first chapter presents an overview of the state of the art in the photoacoustic imaging, the challenges of the technique and the advances and progress achieved. A brief discussion of the problems studied in this thesis is presented.

2. The second chapter is a general review of the physical concepts and mathematical models involved in the photoacoustic imaging.

3. The third chapters presents the arrangement of the measurement technique implemented and the proposal of an algorithm of reconstruction that improves the quality of the photoacoustic images. Several examples to show the capabilities of the algorithm are presented.

4. In the fourth chapter a mathematical model of the photoacoustic electrical signal is exposed, a physical correction that improves the predictions on the shape of the signal is proposed.

5. Finally, the fifth chapter relates the conclusions of the presented work, and a discussion of its potential applications.

Chapter 1

Introduction

It has been observed that, when an optically absorbent material is illuminated with a short pulse ($\sim$ ns) of electromagnetic radiation, an ultrasonic wave is generated; this phenomenon is known as the Photoacoustic (PA) effect, and it was discovered in 1880 by Alexander Graham Bell. If the pulse intensity is low, the PA effect has been modeled as a thermoelastic expansion [1]. When the sample is illuminated, the electromagnetic energy is transferred to the sample and transformed into heat, which provokes a temperature rise in the illuminated region and then an increase in its volume, this change in the sample's mass distribution generates a change in the pressure of its surroundings, a pressure change that, in proper conditions, propagates through the surrounding medium and can be detected by an ultrasound sensor.

The PA effect has had an impact in the areas of physics, mathematics, and biomedical engineering. The main focuses of the PA researches are the spectroscopy and imaging, both accompanied by a high interest in the physical and mathematical modeling of the phenomenon [2]. Because of its potential biomedical applications, the PA imaging has been positioned as an emerging tool that has prompted the research on the PA phenomenon since the mid-1990s [3]. Since then, the PA imaging has made significant progress and achievements, for example, the measurement of finger artery structure and oxygenation [4], gastrointestinal endoscopy [5], molecular imaging [6], and *in vivo* imaging of a rat brain [7]. Another relevant scope in the PA research is the quantitative PA imaging [8]. The PA image is a map of the initial pressure distribution generated by the sample during the scanning, then, it only provides geometrical information of the studied sample; the quantitative PA consists of the recovery of physical information from the source, such as the optical absorption coefficient, from the electrical signal, bringing the capability to recognize different kind of materials, characterized from its optical absorption coefficient, using the PA detection. Then, the quantitative PA imaging pretends to a generate a digital image that brings geometrical information about the structure of the sample but information of the different

1

kind of materials that conforms the sample and its location, it could be a powerful biomedical detection tool. Even though there exist significant advances in the quantitative PA imaging [9], this is still an open problem, which, among other subjects, its solution is based on the physical-mathematical modeling of the PA electrical signal.

In spite of the progress and achievements of the PA imaging, there are challenges and questions to solve to improve the understanding of the technique and its implementation, especially to achieve the clinical translation [10]. The challenges to improve the PA imaging technique are divided in two parts [11]:

1. Scanning systems and detections techniques.

2. The methods and algorithms of reconstruction.

The detection system consists in the array of sensors and its characteristics implemented to measure the PA response of the studied sample, the opportunity areas are: the geometry of the array [12], broadband detection [13], and the characterization of the sensor directivity [14]. The reconstruction method, or inverse algorithms, consists of the process and calculation performed on the electrical signals acquired during the scanning to obtain the desired digital image, the challenges on the reconstruction algorithms are fast performance [15], to improve the contrast and resolution [16], and to avoid the artifact formation [17, 18].

Both the detection technique and the algorithms of reconstruction are highly relevant in the PA imaging research, since the reconstruction algorithms are formulated ad hoc to the measurement technique implemented during the scanning [19]. The main reconstruction methods are the back-projection formulae [20], the eigenfunction expansion [21], and the time reversal [22], while the most common geometries of detection in the PA imaging are the circular and linear for the 2-dimensional case, and the spherical and cylindrical for the 3-dimensional case.

Moreover the geometry, the elements on the array of sensors is an important characteristic of the scanning, because the algorithms of reconstruction are based on the geometrical configuration of the sensors, not considering the number of elements and configuration of the array of sensors in the inversion algorithms leads to artifact formation and low resolution in the image, this statement will be probed in this work. The single-element measurement technique, which consists on the use of just one sensor that is moved through a specific geometry of detection, has been widely used in the PA imaging [23–26], nevertheless, and to the best of my knowledge, an image reconstruction algorithm that considers the single-element measurement technique has not been proposed nor implemented.

In this thesis, these relevant topics of the PA imaging field are investigated. The work presented can be divided in two parts:

1. The proposal of a reconstruction algorithm, based on the back-projection method, and suitable for a measurement technique that involves a single-element scanning over a circular geometry of detection.

2. a 1-dimensional physical-mathematical model of the PA electrical signal, along with the proposal of a correction in the traditional physical modeling of the PA effect.

With the aim to generate a low-cost system to perform a PA scanning and the use of an adequate inversion algorithm to obtain PA images and to study its capabilities, and a mathematical model that can be implemented in the reconstruction methodology to explore the quantitative PA imaging problem, in this thesis:

- A measurement technique is proposed, involving the use of one acoustic sensor and a system that rotates the sample, using a single laser shot per position to generate the PA signal.

- An image reconstruction algorithm is presented, formulated to be suitable for the single-element measurement technique.

- Image reconstructions are presented, using different kinds of samples and geometries, to show the algorithm capabilities to the artifact formation and optimization of the quantitative quality parameters of the images.

- A physical and mathematical model of the 1-dimensional PA effect is developed, proposing a physical correction with that improves the modeling of the PA electrical signal, and with a potential implementation in the PA quantitative analysis.

Chapter 2

Theoretical Background

A brief introduction to the PA effect and its mathematical modeling will be summarized in this chapter. The physical foundations and assumptions that leads to the equation that describes the generation and propagation of the laser-induced ultrasound and the use of this equation to formulate the PA inverse problem will be presented.

The solution to the PA inverse problem is a distribution function that is known as PA image. Two methods to solve the PA inverse problem will be studied: the time reversal method and the back-projection formula, which has a derivation, after physical and mathematical assumptions, that is known as the Delay-and-Sum (DAS) beamforming algorithm. The DAS beamforming algorithm is the basis of the proposed image reconstruction method that is presented in this thesis.

2.1 The photoacoustic effect

The PA effect is the generation of an ultrasonic wave by an optically absorbent material when it is illuminated with pulsed electromagnetic radiation, see figure 2.1. The ultrasonic wave is known as PA pressure or PA wave.

The generation and propagation of the PA pressure have been modeled for ideal fluids, and are adequately described by the coupled equations of heat diffusion for the temperature variation $T(\mathbf{x}, t)$, Eq. 2.1, and the pressure wave equation $P(\mathbf{x}, t)$ [27], Eq. 2.2:

$$\left(\chi \nabla^2 - \frac{\partial}{\partial t} \right) T(\mathbf{x}, t) = -\frac{1}{\rho_0 C_P} H(\mathbf{x}, t), \tag{2.1}$$
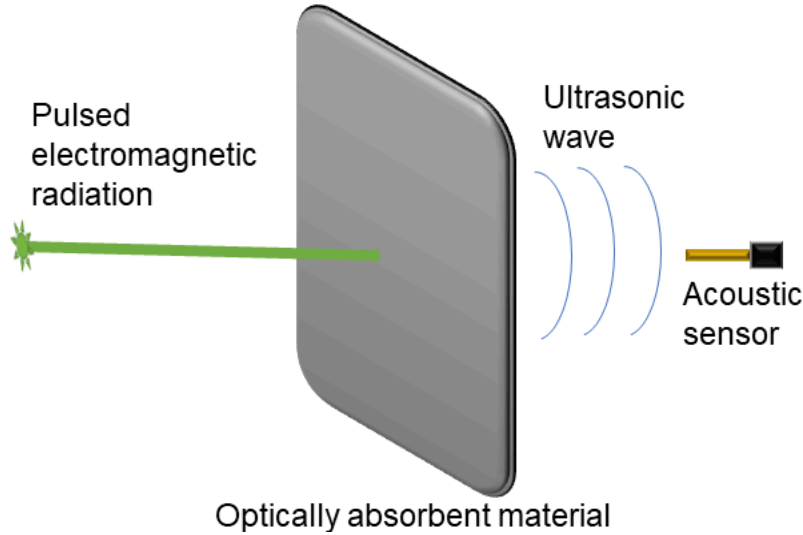
Figure 2.1: Schematic representation of the photoacoustic effect.

$$\left(\frac{1}{K_T\rho_0}\nabla^2 - \frac{\partial^2}{\partial t^2}\right)P(\mathbf{x},t) = -\frac{\beta}{K_T}\frac{\partial^2}{\partial t^2}T(\mathbf{x},t), \tag{2.2}$$

where, for the sample, χ is the thermal diffusivity, C_P the heat capacity at constant pressure, β the thermal expansion coefficient, K_T the isothermal compressibility, and $H(\mathbf{x},t)$ is the electromagnetic energy density per unit time absorbed by the sample. ρ_0 is the mass density of the unperturbed propagation medium.

The electromagnetic energy density per unit of time depends on how the liquid absorbs the optical energy, it is modeled as:

$$H(\mathbf{x}',t) = \mu(\mathbf{x}',t)\phi(\mathbf{x}',t),$$

where $\mathbf{x}'$ represents the position of the PA source, $\mu(\mathbf{x}',t)$ is the optical absorption coefficient of the sample and $\phi(\mathbf{x}',t)$ the laser pulse fluence rate. The fluence rate can be described as the product of the intensity $I(\mathbf{x}')$ and the temporal profile $\theta(t)$ of the laser pulse $\phi(\mathbf{x}',t) = I(\mathbf{x}')\theta(t)$.

2.2   The photoacoustic wave equation

The PA effect is an optical and acoustical problem, and due to the time scale difference, they can be studied as problems independently. The PA wave equation models the propagation of the acoustic wave $P(\mathbf{x},t)$ produced by a thermoelastic expansion of the source.

The PA wave equation is obtained by decoupling the Eqs. (2.1) and (2.2), producing a description of the propagation of the pressure $P(\mathbf{x}, t)$ with a source term that depends on the electromagnetic energy density $H(\mathbf{x}, t)$. There are physical assumptions about the medium where the PA wave propagates: negligible viscosity, the acoustic absorption is ignored, the pressure and density variations are small compared with the initial values, and the particles speed is less than the sound speed.

To decouple the Eqs. (2.1) and (2.2), a physical assumption on the sample is needed, related to its heat diffusion time τ_{th} and the laser pulse time τ_p, it is called the ***thermal confinement condition***: if $\tau_{th} >> \tau_p$, the heat conduction can be neglected [28] ($\nabla T(\mathbf{x}, t) \approx 0$). The thermal confinement implies that the heating is only due to optical absorption and suggests that the heated volume cannot release its temperature excess through the excitation process. When this condition is satisfied, the combination of the Eqs. (2.1) and (2.2) leads to the PA wave equation:

$$\left[\nabla^2 - \frac{1}{c^2} \frac{\partial^2}{\partial t^2} \right] P(\mathbf{x}, t) = -\frac{\beta}{C_P} \frac{\partial H}{\partial t}, \tag{2.3}$$

where c is the sound speed in the medium of propagation, and is defined as $c^2 = \left(K_T \rho_0 - \frac{\beta^2 T_0}{C_P} \right)^{-1}$.

2.3 Photoacoustic inverse problem

The PA inverse problem is a boundary value problem for the PA wave equation, which solution is a spatial distribution function that describes the electromagnetic absorption during the thermoelastic expansion process of the PA effect.

The first assumption to state the PA inverse problem is to consider that the electromagnetic energy density per unit time absorbed by the sample, $H(\mathbf{x}', t)$, can be separated in its spatial and temporal variables, namely:

$$H(\mathbf{x}', t) = h_x(\mathbf{x}')h_t(t).$$

If the sample is illuminated in a time scale τ_p much less than the acoustic wave time of flight, i.e. $\tau_p \ll 1/\mu c$, then, considering that the sample is illuminated at $t = 0$, it can be approximated that [1]

$$h_t \to \delta(t) \text{ as } \Delta T \to 0.$$

The condition $\tau_p \ll 1/\mu c$ is known as the **stress confinement condition** and implies the supposition that the heat is transferred to the sample, through electromagnetic excitation, before its mass density changes.

When the sample is illuminated, the deposited electromagnetic energy is transformed into temperature local changes along with variations in its mass density and the pressure, is satisfied that [1]: $\rho = (K_T P - \beta T)\rho_0$, where ρ_0 is the initial mass density, ρ and p are the changes in the mass density and pressure respectively. When the sample is illuminated (at $t = 0$) the mass density is not changing, then, the thermodynamic relation gives the initial pressure distribution $P\big|_{t=0} = \frac{\beta}{K_T}T\big|_{t=0} = \Gamma h_x$, where Γ is a dimensionless parameter that indicates the efficiency of the heat-to-pressure conversion process, it is called the Grünensein parameter.

To consider stress confinement and the discussed initial pressure distribution, generates a source term equal to $\Gamma h_x d\delta/dt$ in the Eq. (2.3), to solve this equation is equivalent to solve the initial value problem [1]:

$$\left[\nabla^2 - \frac{1}{c^2}\frac{\partial^2}{\partial t^2}\right] P = 0 \quad \text{subject to} \quad P(\mathbf{x}, 0) = \Gamma h_x \quad \text{and} \quad \frac{\partial P}{\partial t}\bigg|_{t=0} = 0. \qquad (2.4)$$

The PA inverse problem is stated from this initial value problem, considering an observation surface S where the set of pressure values $P(\mathbf{x}_S, t)$ is measured, $P(\mathbf{x}_S, t)$ is considered as a boundary condition. Mathematically, the PA inverse problem is [22]:

$$\left[\nabla^2 - \frac{1}{c^2}\frac{\partial^2}{\partial t^2}\right] P(\mathbf{x}, t) = 0, \quad t \geq 0,$$

$$P(\mathbf{x}', 0) = f(\mathbf{x}'), \quad \frac{\partial P}{\partial t}\bigg|_{t=0} = 0,$$

$$P(\mathbf{x}_S, t) = g(\mathbf{x}_S, t) \text{ for } \mathbf{x}_s \in S, \ t \geq 0.$$

With the mathematical model stated, the PA inverse problem is formulated as:

Given the medium sound speed c, and the set of boundary values $g(\mathbf{x}_S, t)$, find the initial value $f(\mathbf{x}')$. This value is the initial pressure distribution that is presented as the PA image.

In addition to the assumptions discussed to state the inverse problem, there are other general assumptions to make the PA inverse problem mathematically solvable: i) the source is assumed to be supported inside S, there are no external PA sources, ii) the homogeneous wave equation is valid in the whole space.

2.3.1 Time reversal method

The time reversal method is a technique that brings a numerical solution to the PA inverse problem. It was suggested by David Finch and Sarah K. Patch [29] for constant sound speed, assuming a PA source located at $\mathbf{x}_0$, whose acoustic waves are detected over a surface S, which location is given by $\mathbf{x}_s$, that encloses a volume V (or an area A in the 2-dimensional case) that contains the PA source. See figure 2.2.
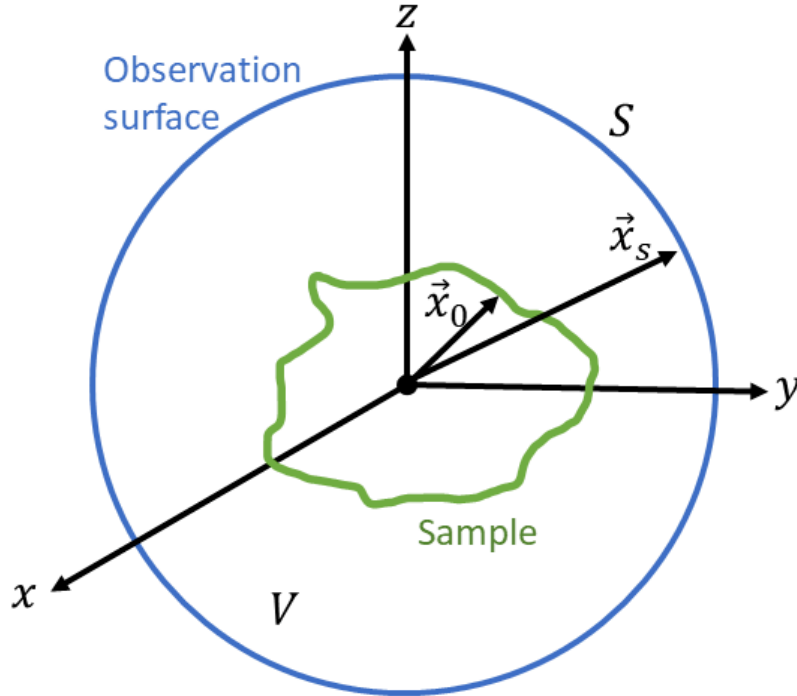
Figure 2.2: Sample and observation surface locations in the mathematical formulation of the time reversal method.

To state the solution to the PA inverse problem through the time reversal method, let $P(\mathbf{x}, t)$ be a solution of the homogeneous wave equation in the initial value problem, Eqs. (2.4), it is proposed that the PA wave has left the volume V in a time τ:

$$\exists\, \tau \;\mid\; P(\mathbf{x}, \tau) = 0, \quad \mathbf{x} \in V.$$

The homogeneous PA wave equation is invariant to time inversion ($t \to -t$), then, at $t = \tau$ the time evolution of $P(\mathbf{x}, \tau)$ is reversed a time τ, obtaining at $t = 2\tau$ the initial pressure distribution. Then, a solution P_{tr} is defined as:

$$P_{\text{tr}}(\mathbf{x}, t) \equiv P(\mathbf{x}, 2\tau - t) \quad t \in [\tau, 2\tau], \quad \mathbf{x} \in V.$$

The function P_{tr} is then a solution to the homogeneous wave equation in the Eqs.

([2.4](#)), and it satisfies:

$$
\begin{aligned}
P_{tr}(\mathbf{x}, \tau) &= P(\mathbf{x}, \tau), \\
\left. \frac{\partial P_{tr}}{\partial t} \right|_{t=\tau} &= -\left. \frac{\partial P}{\partial t} \right|_{t=\tau}.
\end{aligned}
$$

These conditions lead to the relation $P_0(\mathbf{x}_0) = P_{tr}(\mathbf{x}_0, 2\tau)$, where $P_0(\mathbf{x}_0) \equiv P(\mathbf{x}_0, 0)$. In addition, the PA inverse problem involves the knowledge of P_{tr} over the observation surface S, which are the experimental measurements, and are imposed as boundary conditions. Hence, the solution to the PA inverse problem through the time reversal method is posed from the function P_{tr} that satisfies:

$$
\left(\nabla^2 - \frac{1}{c^2} \frac{\partial^2}{\partial t^2} \right) P_{tr}(\mathbf{x}, t) = 0 \quad (\mathbf{x}, t) \in V \times [\tau, 2\tau]
$$

with the initial conditions

$$
\begin{aligned}
P_{tr}(\mathbf{x}, \tau) &= 0, \\
\left. \frac{\partial P_{tr}}{\partial t} \right|_{t=\tau} &= 0 \quad \mathbf{x} \in V,
\end{aligned}
$$

and subject to boundary conditions

$$
P_{tr}(\mathbf{x}_S, \tau) = P(\mathbf{x}_S, 2t - \tau).
$$

The system is solved to find, at $t = 2\tau$, the initial pressure distribution $P_0(\mathbf{x}_0)$.

For the results that will be presented in the Chap. [3](#), the time reversal method was implemented using a third party Matlab$^{©}$ toolbox, called k-Wave [30]. The toolbox was developed for the simulation and reconstruction of PA wave fields, it contains a time domain forward model of acoustic wave propagation for acoustically heterogeneous media with power law absorption [31–33], as well as a fast image reconstruction algorithm based on the time reversal method for an arbitrary shaped measurement surface [34]. The toolbox can be free downloaded from *http://www.k-wave.org*, this website also contains examples and guides to implement the k-Wave toolbox in the PA image reconstruction.

2.3.2   Back-projection method

The back-projection (BP) method is proposed for an experimental configuration that involves a sample (image target) surrounded by a set of detectors that forms an observation surface that encloses the sample. The algorithm is based on the

calculation of the time delay between a point of interest in the image space and each detector position, given a homogeneous sound speed. The line defined by the mentioned point of interest and a detector position in the image space is called projection line [35]; once the projection lines are defined for a desired point of interest (a pixel), the intensity value I_{bp} for this pixel is the sum of the transducers signal at its corresponding time delay, this process is called back-projection [36] and is formulated as:

$$I_{bp}(x,y) = \sum_{i=1}^{N} V_i \left(\sqrt{[x - R\cos\theta_i]^2 + [y - R\sin\theta_i]^2}/c \right), \qquad (2.5)$$

where (x, y) are the Cartesian coordinates of the pixel, N is the number of detectors in the array, which are parametrized to be located at an angular coordinate θ_i, and R is the length of its corresponding projection line, c is the sound speed of the propagation medium. The Fig. 2.3 shows the geometrical configuration of the 2-dimensional case BP method for one projection line and considering a circular geometry of detection. Then, the BP method consists of defining the projection lines for a target in the image space, each projection is back-projected onto this plane and then the plane is rotated an specific angle given by the geometry of the array of transducers and then the process is repeated [37].
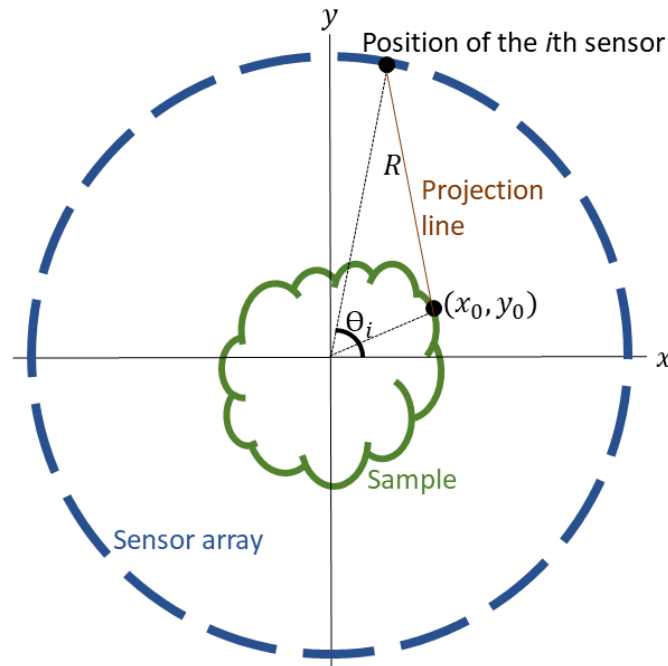

Figure 2.3: Geometrical configuration of the 2-dimensional case of the backprojection method for one projection line, the dotted circle represents the position of the sensors in a circular array of detection.

It is not clear in the literature who proposed the method and when it was implemented for the first time, however, the BP reconstruction algorithm is not exclusive or proposed for PA imaging, it has been traditionally used for a variety of biomedical imaging techniques [38]. Then, this reconstruction method is not originally a solution to the PA inverse problem. Nevertheless, the method and its algorithm has been formulated under some approximations and assumptions to be a solution to this problem, resulting in a set of mathematical relations that defines the BP algorithm as a solution to the PA inverse problem. These mathematical relations are known as the filtered back-projection formulae [1,22].

Each of the BP formulas was obtained for a particular geometry of detection and different physical assumptions of the propagation medium and the PA source, provoking that different formulae brings a different reconstructed image [22]. To solve this disadvantage of the BP method in the PA imaging, a unified formula that considers planar, spherical, and cylindrical detections surfaces; considering a constant sound speed in the propagation medium, was proposed in [20], called the time domain universal back-projection algorithm:

$$P_0(\mathbf{x}_0) = \int_{\Omega_0} b\left(\mathbf{x}, t = |\mathbf{x}_0 - \mathbf{x}|\right) d\Omega_0 / \Omega_0 \qquad (2.6)$$

where, like the time reversal formulation, an observation surface S is defined and Ω_0 is its solid angle with respect to a reconstruction point target $\mathbf{x}_0$, $\mathbf{x}$ is the measurement position and b its BP term related, $b(\mathbf{x}, t) = 2P(\mathbf{x}, t) - 2t\frac{\partial}{\partial t}P(\mathbf{x}, t)$, where $P(\mathbf{x}, t)$ is the pressure detected in S, and $P_0(\mathbf{x}_0)$ is the desired initial pressure distribution. The Eq. (2.6) is clearly written in a BP form, with a similar structure to the Eq. (2.5).

The BP formulae along with the time domain universal BP algorithm makes the traditional BP method to be a formal solution of the PA inverse problem. This methodology for image reconstruction has been widely used in the PA imaging technique [28, 39–41].

2.3.2.1   Delay-and-sum beamforming

The delay-and-sum (DAS) beamforming is a reconstruction algorithm proposed for ultrasound imaging as an implementation of the BP method [42] and is written as

$$y_{\text{DAS}}(\tau_k) = \sum_{i=1}^{N} P_i(\tau_k - \tau_i),$$

where k represents the coordinate of the point of interest in the image space, τ_k is a time index, P_i is the electrical signal acquired by the ith sensor in the array,

formed by N elements, and τ_i is the time that the acoustic wave would take to travel from the point k to the position of the ith sensor. y_{DAS} is called the output of the beamformer and it is the intensity value of the point of interest k in the image. The DAS, being a class of the BP method, supposes that the sample is enclosed by the array of sensors, and the generated ultrasound waves are propagated in a homogeneous medium, which leads to a constant sound speed that is used to calculate the delayed times τ_i.

Although the DAS beamforming was proposed for ultrasound imaging, the algorithm has been used in PA imaging, the adaptation of ultrasound to PA is in the delayed times τ_i: the ultrasound imaging considers the time that the ultrasound wave travels form the actuator/sensor to the sample and, by a process of acoustic reflection, from the sample to the actuator/sensor; while, in the PA imaging, the acoustic wave is generated by the sample, and the time considered is just the time that the acoustic wave takes to travel from the sample to the detector.

2.3.2.2 Synthetic aperture focusing technique

The synthetic aperture focusing technique (SAFT) is an image reconstruction algorithm of the DAS imaging class, it was proposed considering a sensor array where each element is detecting independently and in a different time that the rest of the sensors in the array [43]. In the SAFT, the intensity value of a pixel (I_{SAFT}) located at the position $\mathbf{k}$ in the desired image is calculated following [44]:

$$I_{\text{SAFT}}(\mathbf{k}) = \sum_{i=1}^{N} V\left[\mathbf{s}_i, t - \tau(\mathbf{s}_i, \mathbf{k})\right]_{t=0}, \tag{2.7}$$

where N is the number of elements in the sensor array, $\mathbf{s}_i$ is the position of the ith sensor in the image space, $V\left[\mathbf{s}_i, t\right]$ is the voltage vector acquired by the sensor i during a time t, and τ is the delayed time calculated from the pixel position $\mathbf{k}$ to the position of the ith sensor in the image space, see figure 2.4 for a schematic representation of the Cartesian positions of the sensor and a pixel in the image space.

Even though, being a subclass of the DAS imaging, the SAFT has been implemented in the PA imaging technique, there are critical assumptions made in the SAFT:

1. The elements of the sensor array are assumed to be point-like, then, the best approximation is to consider the position $\mathbf{s}$ as the position of the sensor centroid.

2. The point-like approximation leads to consider the sensor to be omnidirectional.

3. The medium of propagation is homogeneous and acoustically non-absorbent. These approximations provokes that the SAFT image is affected by artifacts and a low resolution.

The main type of artifacts formed in the SAFT images are the side-lobe artifacts, and are due to the high sensibility of the algorithm to off-axis signals [45]. According to the Eq. (2.7), in the SAFT process, each sensor of the array contributes to every pixel in the image, even though not necessarily every sensor detects a signal from any region of the observation surface.

To avoid the artifact formation in the SAFT and DAS algorithms, proposals of new reconstruction methods emerged as a modifications of the DAS-SAFT algorithm such as the delay-multiply-and-sum (DMAS) [46], the DMAS with coherence factor [47], and the double-stage DMAS [45].
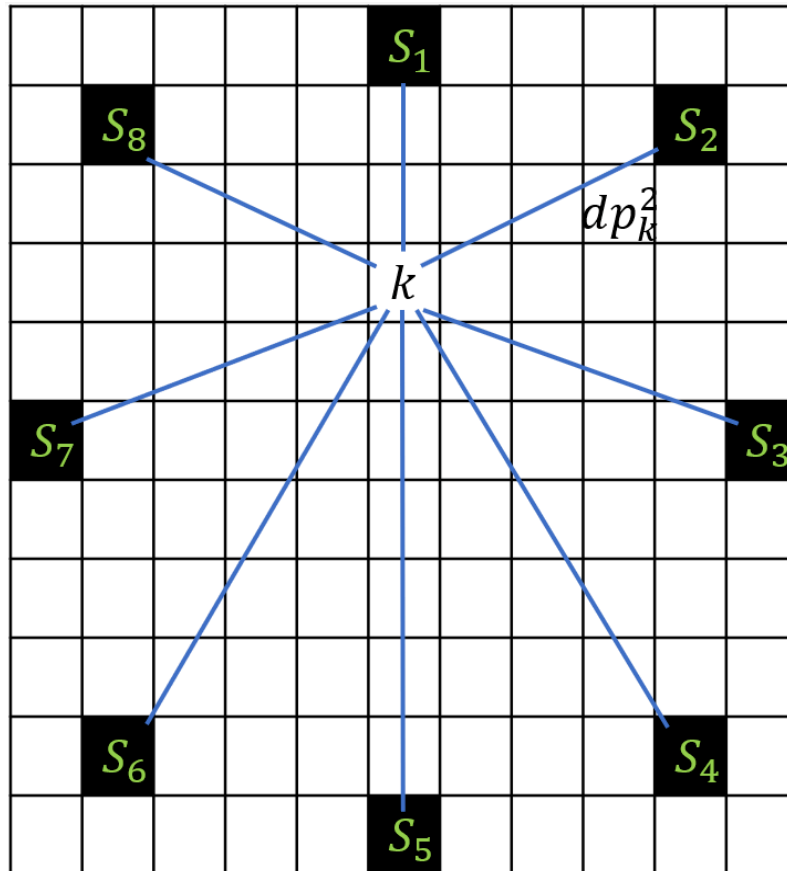

Figure 2.4: Image space and the locations of a circular sensor array of eight elements. The blue lines represent the distance related to the time delays associated to a pixel k.

Chapter 3

Single sensor photoacoustic imaging

A novel image reconstruction algorithm is proposed, based on the SAFT and suitable for a particular experimental configuration that involves a tomographic scan using a single acoustic sensor and a mechatronic system that rotates the sample Considering that the SAFT was proposed in ultrasound for a single transducer scanning and, the technique and its delay-and-sum variants have been adapted to PA imaging when an array of sensors are used, the proposed method is called Single Sensor Scanning Synthetic Aperture Focusing Technique (SSC-SAFT). Besides, this method considers the effective area of detection of the acoustic sensors, and the measurement technique favors that the detection is in the direction of the maximum directivity of the sensor, avoiding the assumptions of an omnidirectional and punctual sensor.

In the SSC-SAFT, it is proposed to perform the image reconstruction following the SAFT ideas but considering exclusively the sensor detection region, performing, in some fashion, a segmented reconstruction, where every segment (or region) is delimited by the size, position, and the area of detection of the acoustic sensor in the image grid.

3.1 The single sensor measurement technique

The experimental configuration involved in the physical foundations of the SSC-SAFT method is presented in the Fig. (3.1). A lab-made PVDF based sensor with a circular sensing surface with 1 mm of diameter was used to perform the scanning ($A = 1$mm), an optical fiber was used to guide the emitted pulse of a Nd-YAG Q-switched laser, with a pulse duration of 10 ns, emitting at 532 nm of wave-

length. The sample was placed in a sample-holder connected to a stepper motor, so that the sample can be rotated around an axis coincident with the center of the sample-holder. The system is submerged in a water tank so the acoustic impedance-matching is achieved.

The acquisition system is an USB scope Analog Arts SA985, with a sampling rate of 100 MHz, programmed to save the electrical signal each time the laser is fired. An Arduino board is used to control the system, generating a TTL signal to habilitate the laser and control the activation of the stepper motor. Once the sample is collocated in the holder and the sensor and optical fiber is placed in the water tank, the distance between the detection face of the sensor and the axis of rotation is measured. The first step to perform the PA tomography is to fire the laser beam, once the sample is illuminated with a single pulse, the electrical signal is acquired and stored, then, the sample is rotated 1.8 sexagesimal degrees ($\pi/100$ rad) and the process is repeated 200 times, so a circular surface of observation is emulated.
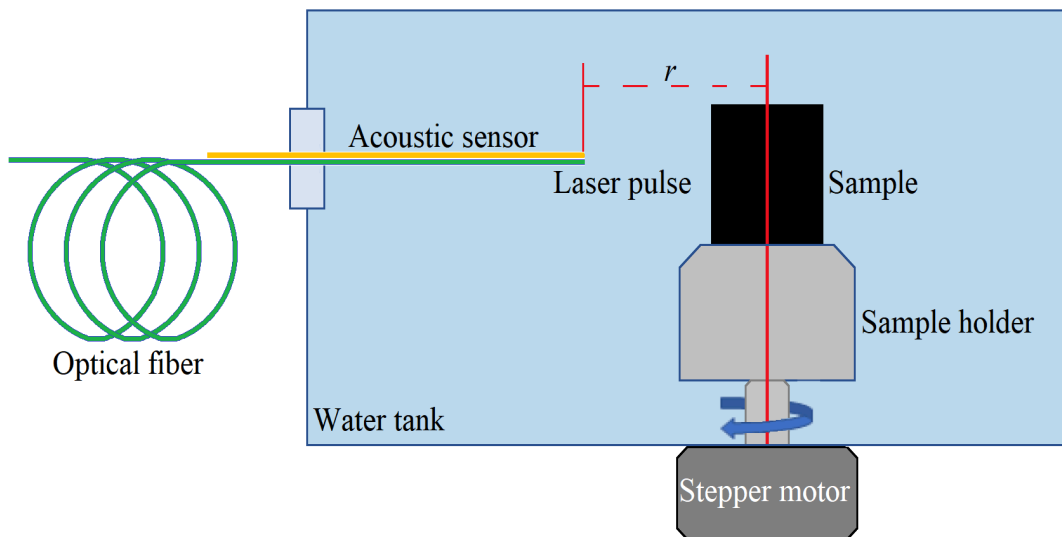
Figure 3.1: Schematic representation of the PA tomograph. The scanning is achieved with one acoustic sensor and a rotation of the sample, the signals are acquired with a single laser pulse.

The electrical signal acquisition was performed by Prof. Luis Polo-Parada at Dalton Cardiovascular Research Center of the University of Missouri. Once the electrical signals were acquired and stored, the image reconstruction was performed in a computer with a 64 bit CPU (Intel(R) Core i7-10700K) at 3.8 GHz, 32GB RAM and without a GPU board.

3.2 The single-sensor scanning synthetic aperture focusing technique: a proposed method for photoacoustic image reconstruction

3.2.1 The computational grid

The PA image is a matrix where each element represents the position of a pixel, and its numerical entry the grayscale or intensity value. The method aims to calculate this numerical entry for each element of the matrix based on the electrical signals acquired during the PA scanning. As a result, an intensity image that represents the initial pressure distribution that generates those electrical signals is obtained. This matrix, in conjunction with its physical attributes, is called the computational grid.

The computational grid represents the region of space where the PA scanning occurs, in the case of a circular scanning, a square matrix is the optimal shape. The elements to build the computational grid are: the number of nodes (entries), $Nx \times Nx$ in the case of a square grid, and the horizontal (and then vertical) spatial length x that the grid spans. Considering the single sensor scanning discussed in this methodology, let r be the distance between the axis of rotation of the sample and the detection area of the sensor, then, the minimum length that the grid must cover is $x_{min} = 2r$, note that, in the case of a circular array of sensors, r is just the radius of this array.

Considering a computational grid of Nx nodes per side, and x, the length that covers, the spatial resolution of the grid, meaning the size of a single pixel in the image, is $\Delta x = x/Nx$. Therefore, given a fixed x, the greater Nx is, the higher the resolution. To set a proper number of nodes in the grid, it is necessary to consider the sampling interval given by the acquisition system, as the computational grid is the discretization of the region of space where the measurements are performed, then the minimum size of a pixel can be expressed as

$$\Delta x_{min} = c\Delta t \quad \text{or} \quad \Delta x \geq c\Delta t,$$

where Δt is, by Nyquist sampling theorem, the double of the temporal sampling interval, and c is the mean sound speed of the medium. Since $\Delta x = x/Nx$ and $x_{min} = 2r$, a condition for the number of nodes in the computational grid can be established as:

$$Nx \leq \frac{r}{c\Delta t} \quad \text{or} \quad Nx \leq f\frac{r}{c}, \tag{3.1}$$

where f is the Nyquist frequency, half of the sampling rate. Therefore, the image resolution is delimited by the data acquisition frequency and the distance between

sample and detector.

3.2.2   Image formation

Once the computational grid is constructed, the positions of the sensor centroid during the scanning are located on it, let $\mathbf{s}_i$ be the ith position of the sensor centroid, then, the SAFT reconstruction is performed over the line of pixels that connects $\mathbf{s}_1$ and the position of the axis of rotation of the sample, Fig. 3.2 (a). This process is repeated for every position $\mathbf{s}_i$, obtaining an image of N lines, N being the number of positions of the sensor, that connects the position of the axis of rotation and the boundary of the detection surface formed by the sensor positions, Fig. 3.2 (b).The number of pixels of a line described in this step of the process depends on the number of nodes of the computational grid, let M be the number of pixels of a line of reconstruction, then, the grayscale value of the pixel j in the line l_i corresponding to the position $\mathbf{s}_i$ is:

$$I_{\text{SSC-SAFT}}\left(l_i^j\right) = V\left[\mathbf{s}_i, t - \tau\left(\mathbf{s}_i, l_i^j\right)\right]_{t=0}, \tag{3.2}$$

for $j = 1, 2, \cdots M$, where V is the voltage vector acquired during a time t by the sensor whose centroid is in the position $\mathbf{s}_i$. l_i^j represents the position of the pixel j in the line i, with τ being the corresponding time delay calculated as in the SAFT procedure.

In addition to having considered the position of the sensor centroid, the next step is to look up its effective area of detection in the image reconstruction plane, then, it is necessary to calculate the number of pixels that covers this portion of the computational grid. Since the reconstruction is performed in a plane, the image obtained can be understood as an image of a slice of the sample, the portion of the sensor involved in this plane of reconstruction is the length considered in this method. Let A be the length of this mentioned segment, the number of pixels that it covers is $A/\Delta x$. The reconstruction procedure described in the Eq. (3.2) is repeated for as many contiguous lines as the rounded value of $A/\Delta x$, considering now, instead of $\mathbf{s}_i$, the positions $\mathbf{s}_{i,k}$, where i is a label to describe the ith position of the sensor, and k is an index to describe the coordinates of the pixel that conforms the effective region of detection discussed, see Fig. 3.2 (c), generating a segmented region of reconstruction that encompasses the portion of the sample that was illuminated and its corresponding detection surface. Following these ideas, the intensity value ($I_{\text{SSC-SAFT}}$) of a pixel in a PA image obtained by the SSC-SAFT reconstruction method can be summarized in the following relation:

$$I_{\text{SSC-SAFT}}\left(l_{i,k}^j\right) = V\left[\mathbf{s}_i, t - \tau\left(\mathbf{s}_{i,k}, l_{i,k}^j\right)\right]_{t=0}, \tag{3.3}$$
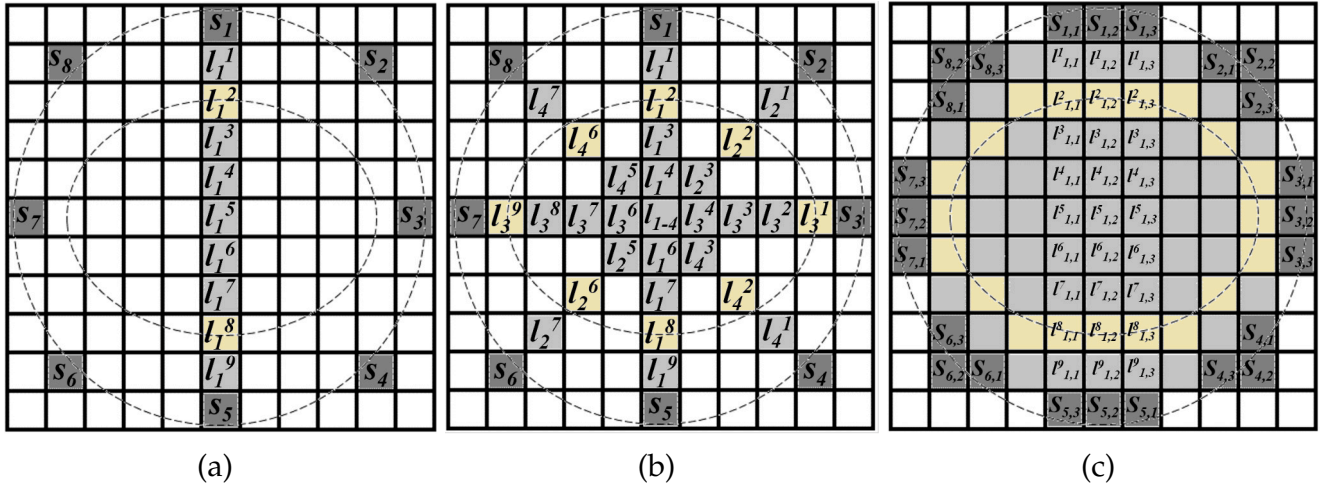
Figure 3.2: Schematic representation of the SSC-SAFT process. **(a)** Perform the SAFT reconstruction on the line l_1 of pixels that connects the position of the sensor centroid $\mathbf{s_1}$ with the position of the axis of rotation. **(b)** Repeat step (a) for the rest of the sensor positions. **(c)** For each sensor position $\mathbf{s}_{i,k}$, repeat the SAFT reconstruction over the neighboring line $l^j_{i,k}$ so the effective area of detection of the sensor is covered in the grid. To avoid crowding in the figure of step (c), the labels $l^j_{i,k}$ are shown only for the case of the sensor $\mathbf{s}_{1,k}$.

for $j = 1, 2, \cdots M$ and $k = 1, 2, \cdots \text{round}(A/\Delta x)$]. k is the position of a pixel that conforms the effective region of detection, with length A, of the referred sensor position in the computational grid. $l^j_{i,k}$ is the pixel j on the line of pixels $l_{i,k}$, formed by M pixels, that connects k with the pixel position of the axis of rotation, τ is the corresponding time delay for a given medium speed of sound. $\text{round}(A/\Delta x)$ is the rounded value of A divided by Δx, recalling that Δx is the size of a pixel obtained when the computational grid is defined. The process is performed for every pixel k in the line $l_{i,k}$, and repeated for every value of k, the sensor size is covered by considering all the values of k that fills the space occupied by the sensor, and then, the calculation is repeated for every sensor position $\mathbf{s}_i$. Fig. 3.2 is a representation of the SSC-SAFT process for the case of a circular scanning achieved with 8 positions of the sensor ($i = 1, 2, \cdots 8$). In this example, the dotted circle represents the path covered by the sensor when moving during the scanning, and the dotted ellipse represents the position of the source to be reconstructed. The square computational grid has 121 entries ($Nx = 11$), the sensor has a region of detection equal to 3 pixels of length ($k = 1, 2, 3$), where $\mathbf{s}_{i,2}$ corresponds to the barycenter of the ith position of the pixel, in general, $\mathbf{s}_{i,b} = \mathbf{s}_i$ with $b = \text{round}(A/2\Delta x)$.

Because of the implementation of the SAFT reconstruction over a line of pixels, the intensity value of a pixel is not a sum of voltage values, instead, this is di-

rectly related to the voltage amplitude of the signal acquired by the sensor in the position involved. Then, the variation of the intensity value of the pixels in the line is proportional to the waveform of the signal used to reconstruct the image. In addition, the high sensibility of the SAFT reconstruction to off-axis signals is avoided, and then, the side-lobe artifacts and comet-tail signs are removed.

3.2.3   Processing complexity

Following the described notation, the number of operations to perform the reconstruction over a line is $2r/\Delta x$, in the second step of the reconstruction, the number of operations required are N times the operations for a line of reconstruction, that is $(2r/\Delta x)N$, and then, the number of operations to perform the SSC-SAFT is $(A/\Delta x)(2r/\Delta x)N$. Recalling that $\Delta x = x/Nx$ and $x_{\min} = 2r$, the number of operations to recover a PA image through the SSC-SAFT is $(NA/\Delta x)Nx$. For the SAFT, the operations required are $(N)Nx^2$, therefore, the order of computational complexity of the SAFT is $O(Nx^2)$, and for the SSC-SAFT is $O(Nx)$, which is an exponentially lower computational cost that will lead in a faster performance.

3.3   Capabilities of the proposed method

This section presents the PA images obtained with the proposed SSC-SAFT method, for a numerical calculation and an experimental scanning, using the measurement technique presented in the sec. 3.1. The PA images obtained with the SSC-SAFT method will be compared qualitatively and quantitatively with those obtained using the DAS-SAFT, which is the basis of the proposed method, and the time reversal method, which is a robust inversion method based on the PA wave equation. The reconstruction through the time reversal method was achieved using the MATLAB toolbox k-Wave [34].

The characteristics of the recovered images that will be evaluated are

- The artifact removal

- Spatial resolution

- Definition

- The recovering targets in the image with a low signal-to-noise ratio (SNR) of the electrical signals

The distance r between the axis of rotation and the detection surface was measured through a photograph of the experimental setup using the software *ImageJ*

(https://imagej.nih.gov/ij/), the spatial size of the computational grid x was calculated as $x = 2r + r/10$. The measurement system was submerged in water and backward signals were acquired, so the mean sound speed of the medium was set to 1500 m/s. Nx was calculated using the Eq. (3.1).

The images were normalized so their intensity values are between 0 and 1, the color bar used is one that maps the intensity value 0 to the color black, and the intensity 1 to the color withe, the values between them are presented in shades of red, see Fig. 3.3.

Figure 3.3: Color bar used to indicate the mapping of the intensity values displayed in the images.

To quantitatively compare the quality of the images, the lateral variation profile (LVP) of an image will be presented, it was calculated following the relation

$$I_{dB}(j) = -20\log_{10}\left(\frac{I_{max}}{I(j)}\right),\tag{3.4}$$

where $I(j)$ is the intensity of the pixel j in the studied image section with I_{max} its maximum intensity, $I_{dB}(j)$ is the resulting amplitude (or power, following the notation in [45]) in decibels. The resulted vector is a description of the variation of the pixel intensities in a determined region of the image and it brings relevant information such as the full width at half maximum (FWHM) of a target and the side-lobe levels in the profile. The FWHM describes how much an object in the image spreads out, then, the lower the FWHM the higher the quality of the image. On the other hand, the side-lobe levels represent the artifact formation in the studied section of the image, then, the lower the side-lobe levels, the higher the image quality.

Another important parameter to quantitatively evaluate the quality of an image is the signal-to-noise ratio, the higher the SNR the higher the image quality. This parameter was calculated form the whole image using the relation

$$\text{SNR}(I) = 20\log_{10}\left(\frac{I_{max} - I_{min}}{\sigma(I)}\right),\tag{3.5}$$

where I is the digital image, I_{min} its minimum intensity, and $\sigma(I)$ its standard deviation. The last parameter that will be presented from the reconstructions performed is the processing time, which does not affect the quality of the image but its important when real-time imaging wants to be achieved.

3.3.1   Artifact removal: isolated acoustic particle, a numerical calculation

The Green function for the PA wave equation in space, for a thermal point-like particle [48, 49], was used to calculate the forward problem. Here, it is proposed that the measured pressure p in $\mathbf{x}$ at the time t, generated by a single PA source of acoustic diameter d_0 whose center is in $\mathbf{x}'$ is described by [50]

$$p(\mathbf{x} - \mathbf{x}', t) = p_0 \frac{ct - |\mathbf{x} - \mathbf{x}'|}{|\mathbf{x} - \mathbf{x}'|} \exp\left[-\left(\frac{ct - |\mathbf{x} - \mathbf{x}'|}{d_0/2} \right)^2 \right] \qquad (3.6)$$

where c is the medium sound speed, $p_0 = \alpha/d_0^3$ is the initial pressure generated by the particle, with α being a parameter that depends on the energy per laser pulse, the sound speed and the heat capacity at constant pressure of the propagation medium, and the thermal expansion coefficient of the particle.

Equation. 3.6 is a good approximation of the thermoacoustic pressure for a thermal particle, and here it was used to calculate the PA response generated by an acoustic particle of 500 μm diameter, measured in different positions over a circular path. It is important to highlight that this numerical example aims to analyze the resulting image of the simplest case of an ideal particle located in the center of the observation surface. The numerical calculation was performed considering a sampling rate of 100 MHz, moving the observation position ($\mathbf{x}$) over a circular path of 5 mm of radius, covered with 40 equidistant positions, and a medium sound speed of 1500 m/s. This procedure is not focused on the quantitative capabilities of the PA imaging, then the value of p_0 in the Eq. (3.6) was set to 1 Pa, as this just modulates the amplitude of the solution. The finite sensor signal was constructed following the approximations discussed in the Sec. 3.2.2, and calculated so that the sensor positions covered the perimeter of the circular sensing surface, the resulted sensor length is 788 μm. The conditions have been idealized to be a proof of concept of the proposed image reconstruction method.

Once the forward problem was calculated, the solutions were used to perform the image reconstruction with the DAS-SAFT, time reversal, and the SSC-SAFT methods. Following the notation and relation given in the Eq. (3.1), the parameters defined to carry out the reconstruction are: $r = 5$ mm, $Nx = 333$, and $\Delta x = 31.5$ μm. The resulted images are shown in the Fig. 3.4 (a)-(c). The processing time to obtain the grayscale images are: 4.8 s for time reversal, 11.3 s for DAS-SAFT, and 1.6 s for SSC-SAFT.

The images obtained reveal that, DAS-SAFT and time reversal result in a distinguishable object in the image at the expense of high levels of side lobe artifacts, while the SSC-SAFT removes completely this kind of artifacts, resulting in a more
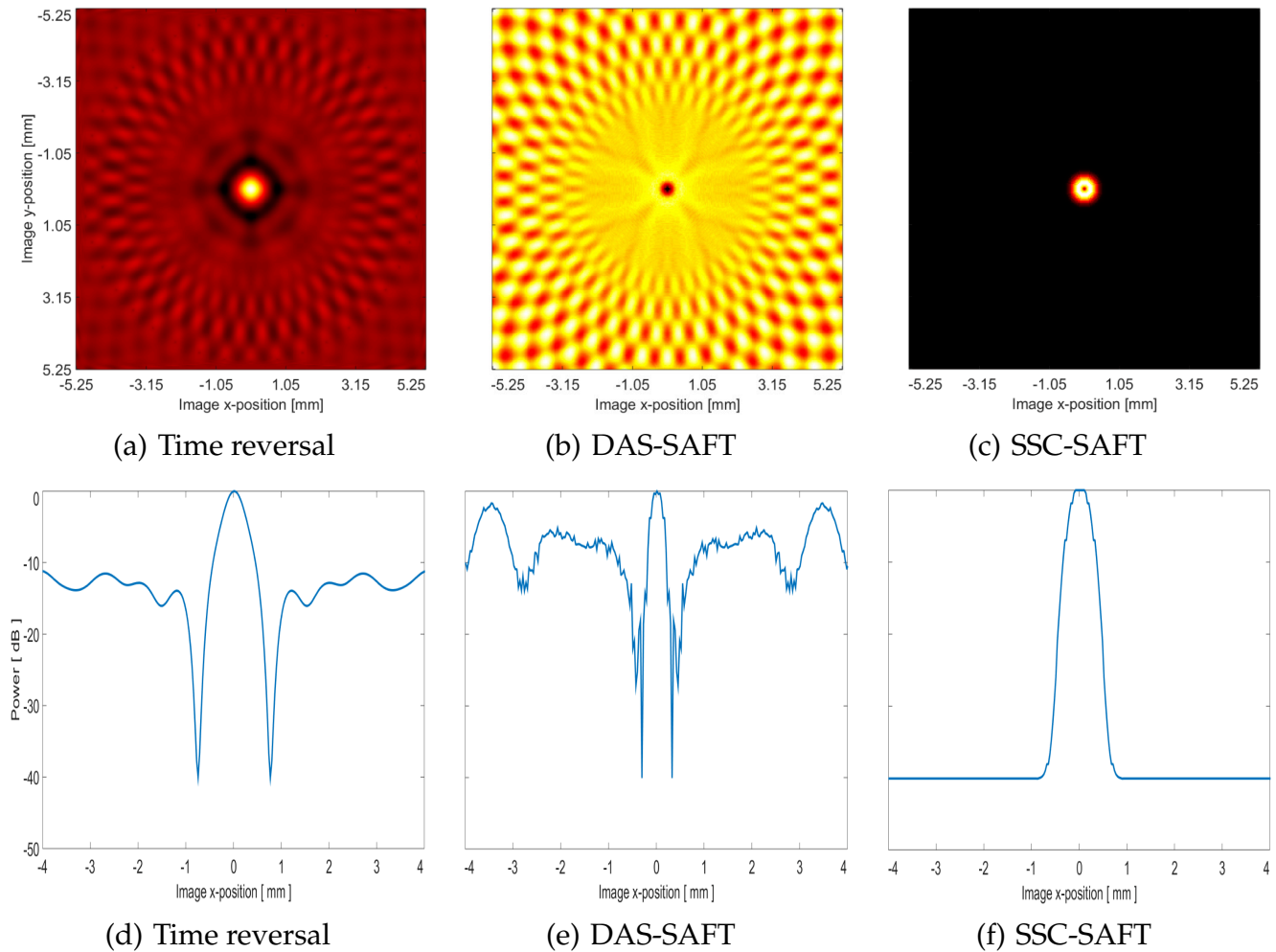
Figure 3.4: (a)-(c) Photoacoustic image using the reconstruction method indicated. (d)-(f) Lateral variation profile of the region containing the sample, at -189 μm depth (y-position) from -4.0 to +4.0 mm of lateral path in the image x-position.

clear and high contrast target. To quantitatively compare the quality of the images, the LVP of the images, in the region that contains the target and in a lateral path from -4.0 mm to $+4.0$ mm of the image x-position, are presented in the Fig. 3.4 (d)-(f).

According to the LVP, the side-lobe levels of the time reversal image is about -13.93 dB for the lower and -11.53 dB for the higher, for DAS-SAFT the range is -18.07 dB to -1.69 dB, and, as mentioned, the SSC-SAFT image is free of side-lobe artifacts. In addition, the FWHM was estimated, obtaining 1214 μm for time reversal, 572 μm for DAS-SAFT, and 927 μm for SSC-SAFT.

The removal of the side-lobe artifacts is a qualitative characteristic of the SSC-SAFT image that improves the quantitative quality parameters. The side-lobe

artifacts in the DAS-SAFT and the time reversal images distort the recovered object and, even though this is a numerical calculation, without electrical noise, the images and its LVP are noisy. As will be demonstrated, the side-lobe artifacts could affect the spatial resolution and definition of the reconstructed objects in the image, disfavoring the correct interpretation of the result and hindering a digital image processing.

3.3.2   Spatial resolution: separate copper wires

To evaluate the recovered spatial lengths of an object in the reconstructed image, a sample that consists of three copper wires separated, and placed as shown in Fig. 3.5, were scanned. The copper wires were covered with black liquid tape to improve the light absorption and then the SNR of the acquired electrical signals. Because the wires were separated and of small length compared with the imaged area, the effect of the isolated particle discussed in the Sec. 3.3.1 will be achieved, but now, with objects collocated out of the axis of rotation.
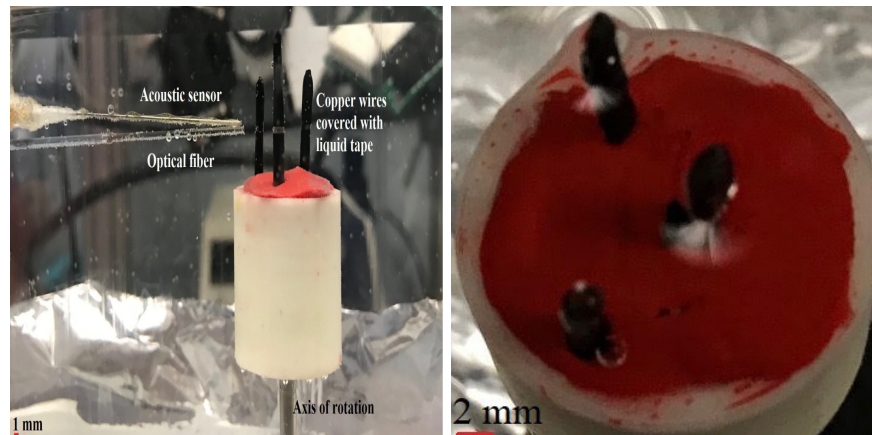

Figure 3.5: Photography of the sample scanned with the photoacoustic tomograph. The sample consists of three copper wires separated and covered with liquid tape.

The quality of the electrical signals has an important influence on the reconstructed image. A useful representation of the raw time-series data is the sinogram, which allows to evaluate the quality of a set of electrical signals. To form the sinogram, the electrical signals are stored in rows, and the time steps are transformed into a spatial length that matches with the image spatial resolution (a pixel), obtaining a spatial representation of the voltage amplitude as a grayscale value and as a function of the angle of rotation during the experiment.

The sinogram obtained with the electrical signals acquired during the PA scanning is presented in the Fig. 3.6 and reveals the appearance of three regions of high peak-to-peak voltage amplitude, located approximately at $0°$, $90°$ and $270°$, which, as expected, are due to the PA signal generated by the three copper wires.
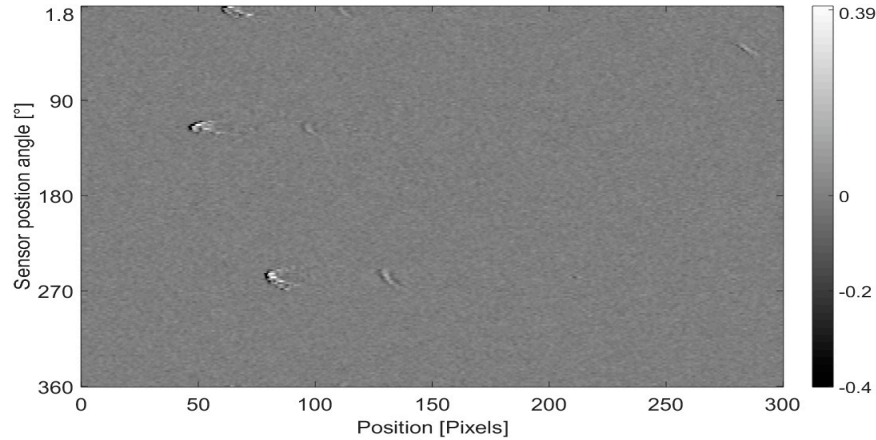

Figure 3.6: Sinogram of the electrical signals acquired during the scanning. The grayscale values correspond to the voltage amplitude of the signals.

The distance between the sensing area and the axis of rotation was $r = 9$ mm, then, the computational grid parameters to perform the image reconstruction were $x = 18.9$ mm, $Nx = 300$, and $\Delta x = 63$ μm. The results are presented in the Figs. 3.7.

Three objects can be noticed in the images, corresponding to the three copper wires. Because of the backward and single-sensor measurement, the whole perimeter of the wires is not recovered, this can be seen from the sinogram, nevertheless, the curvature of the wires is recovered in the SSC-SAFT images, while the DAS-SAFT and time reversal images distort it and suffers from the formation of side-lobe artifacts.

From the sinogram, the high SNR of the electrical signals can be noticed, this allows to set a threshold on the set of signals to differentiate the PA information from the noise, at the expense of losing the bipolar characteristic of the signal maintaining its time-of-flight and positive waveform, that will lead in a higher contrast and better definition of the objects in the image. Then, a simple thresholding set at $+0.06$ V was applied to the electrical signals and the result was used to perform the image reconstruction, the results are presented in Figs. 3.8 (a)-(c).

The contrast enhancement can be noted, as well as the artifact formation effect that was shown numerically in Sec. 3.3.1, and how the SSC-SAFT successfully corrects them. The shape distortion in DAS-SAFT and time reversal is clear as

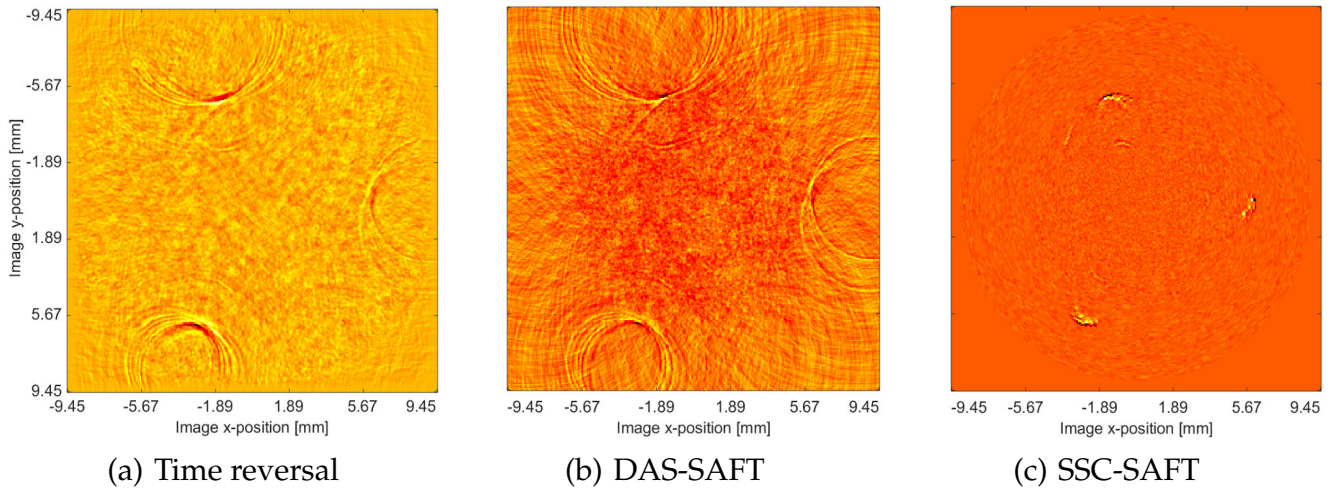(a) Time reversal   (b) DAS-SAFT   (c) SSC-SAFT

Figure 3.7: Resulted images using the reconstruction method indicated.

well as how SSC-SAFT preserves the curvature of the samples. To quantitatively evaluate the quality of the images, the LVP was calculated using the Eq. 3.4 for the region that contains the copper wires located at a depth of $-916\,\mu$m of the image x-position and from -5.53 to -2.00 mm of the image y-position. The resulted profiles are shown in the Figs.3.8 (b)-(d).

The region studied contains two objects, the two faces of the copper wire that were illuminated during the experiments, so a LVP with two prominent peaks is expected. The quality parameters calculated from the profiles, and the SNR calculated form the whole image, are presented in the table 3.1. The FWHM was estimated from the first peak, the one that is better defined in the three cases.

Quality parameter	Time reversal	DAS-SAFT	SSC-SAFT
Side-lobe level (dB)	-11.12, -3.30	-21.05, -8.01	–
FWHM (μm)	441	693	121
SNR (dB)	68.12	59.45	78.24
Processing time (s)	6.5	51.0	0.2

Table 3.1: Quantitative parameters from the intensity images obtained. The side lobe levels and FWHM were estimated from the lateral variation profile. The SNR was calculated from the whole image.

The removal of the side-lobe artifacts is a qualitative characteristic of the SSC-SAFT resulted image, now the LVP numerically demonstrated this, the DAS-SAFT image is the most affected by these artifacts, and its profile shows how the object is considerably distorted.

(a) Time reversal (b) DAS-SAFT (c) SSC-SAFT

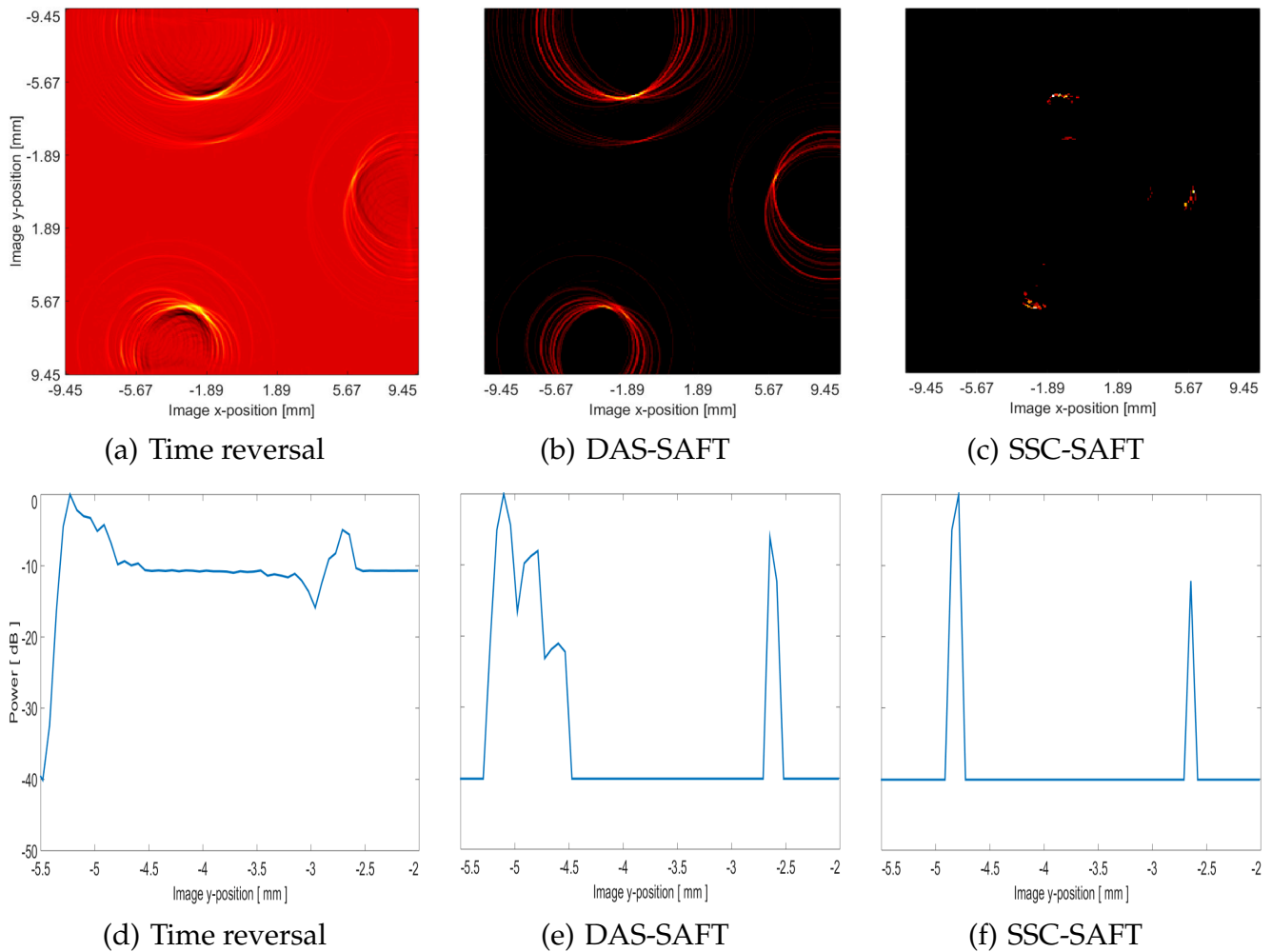(d) Time reversal (e) DAS-SAFT (f) SSC-SAFT

Figure 3.8: (a)-(c) Resulted images after the signal thresholding and using the reconstruction method indicated. (d)-(f) Lateral variation profiles for the region at -916 μm of the image x-position and from -5.53 to -2.00 mm of the image y-position.

As described, the LVP has been calculated from the region of the image that contains the two illuminated faces of one of the wires, then, the distances between the two prominent peaks in each LVP brings the spatial dimensions recovered for the studied target, these lengths are the following: 2.5 mm for time reversal, 2.5 mm for DAS-SAFT, and 2.1 mm for the SSC-SAFT, while the actual length of the wire, measured from the photography with the software *ImageJ*, is 2.0 mm. Time reversal and DAS-SAFT provides an accurate resolution, nevertheless, the image obtained through the proposed SSC-SAFT provides a lower discrepancy between the recovered and the actual dimensions of the studied object.

The SSC-SAFT image has a lower FWHM and a LVP without artifacts, favoring

the definition and correct interpretation of the reconstructed objects in the image and providing a better spatial resolution.

3.3.3   Definition: contiguous copper wires

Along with the spatial resolution, another important qualitative parameter that improves the image quality is the objects definition in the image, which refers as how the actual shape of the sample is recovered in the reconstructed image. To evaluate this parameter, copper wires were used and placed next to each other forming a hollow cylinder, see Fig. 3.9.
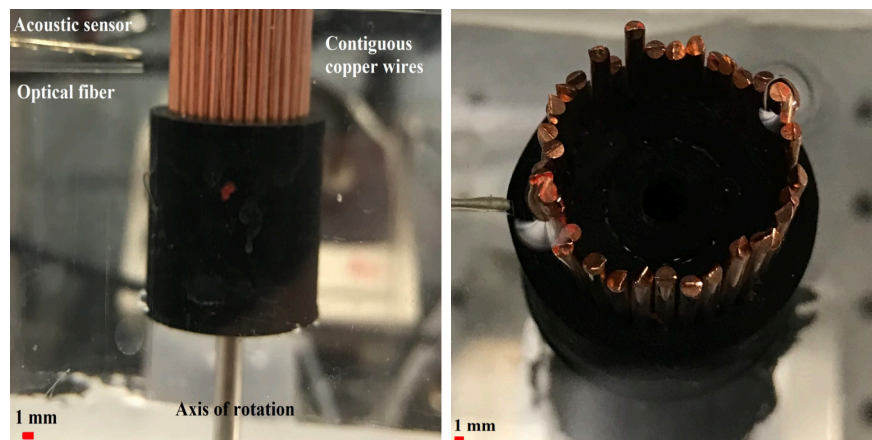

Figure 3.9: Photography of the sample scanned with the photoacoustic tomograph to study the definition of the objects in the reconstructed image. The sample consists of contiguous copper wires forming a hollow cylinder.

Because the recovered object in the image corresponds to the cross section of the illuminated region of the sample, the expected geometry of the reconstructed object is a circle-like pattern. To evaluate the definition in the image, the curvature of the illuminated face of a copper wire should be identifiable in the reconstructed image. The sinogram obtained from the electrical signals acquired is presented in the Fig. 3.10.

As the sinogram is a spatial representation of the voltage amplitude as a function of the angle of rotation, when a circular pattern is expected in the reconstructed image, a vertical line of higher intensity than the background should be formed in the sinogram, this pattern can be noticed, as well as the separation and curvature of each copper wire, then, these characteristics must be inherited in the image.

During the PA scanning, the distance between the sensing face and the axis of
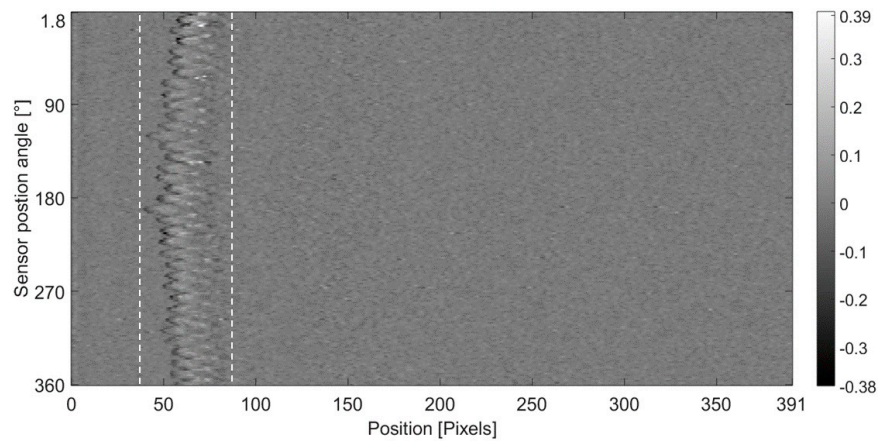
Figure 3.10: Sinogram of the electrical signals acquired during the scanning of the contiguous copper wires. The region between the dotted lines represents the region of interest. The grayscale values correspond to the voltage amplitude of the signals.

rotation was $r = 11.7$ mm, then, the computational gird parameters was $x = 24.6$ mm, $Nx = 391$, and $\Delta x = 63$ μm. A threshold set at $+0.03$ V was used, and, because of the nature of the experiment and the pattern noticed in the sinogram, the reconstruction was focused defining a Region Of Interest (ROI) on the sinogram from the position 35 to 90 pixels, highlighted between the dotted lines in the Fig. 3.10. The resulted PA images are shown in the Figs. 3.11 (a)-(c).

The circle-like pattern is recovered by the three methods and, as the experiment presented in the Sec. 3.3.2, because of the measurement technique, the entire perimeter can not be recovered, just the illuminated region. The SSC-SAFT recovers the curvature of the copper wires, while the time reversal and DAS-SAFT methods distort them. To quantitatively evaluate the quality of the images, the LVP for the region at a depth of 0.00 mm of the image y-position and from -11.00 mm to $+11.00$ mm of the image x-position was studied. This region contains two of the copper wires in the sample, so two prominent peaks are expected. The resulting profiles are presented in the Figs. 3.11 (d)-(e).

The analysis of the FWHM of the first prominent peak, corresponding to one of the copper wires, the side-lobe level of each LVP, and the SNR of the image are presented in the table 3.2. The removal of the side-lobe artifacts is clear for the SSC-SAFT, achieving a decrease of 23% and 60% of the FWHM and an increase of 21% and 32% of the SNR compared with time reversal and DAS-SAFT respectively, providing an image of better quality.

It can be seen how, for the time reversal and DAS-SAFT images, the side-lobe artifacts of a single copper wire overlaps with those of the contiguous wire, distorting

(a) Time reversal　　　(b) DAS-SAFT　　　(c) SSC-SAFT

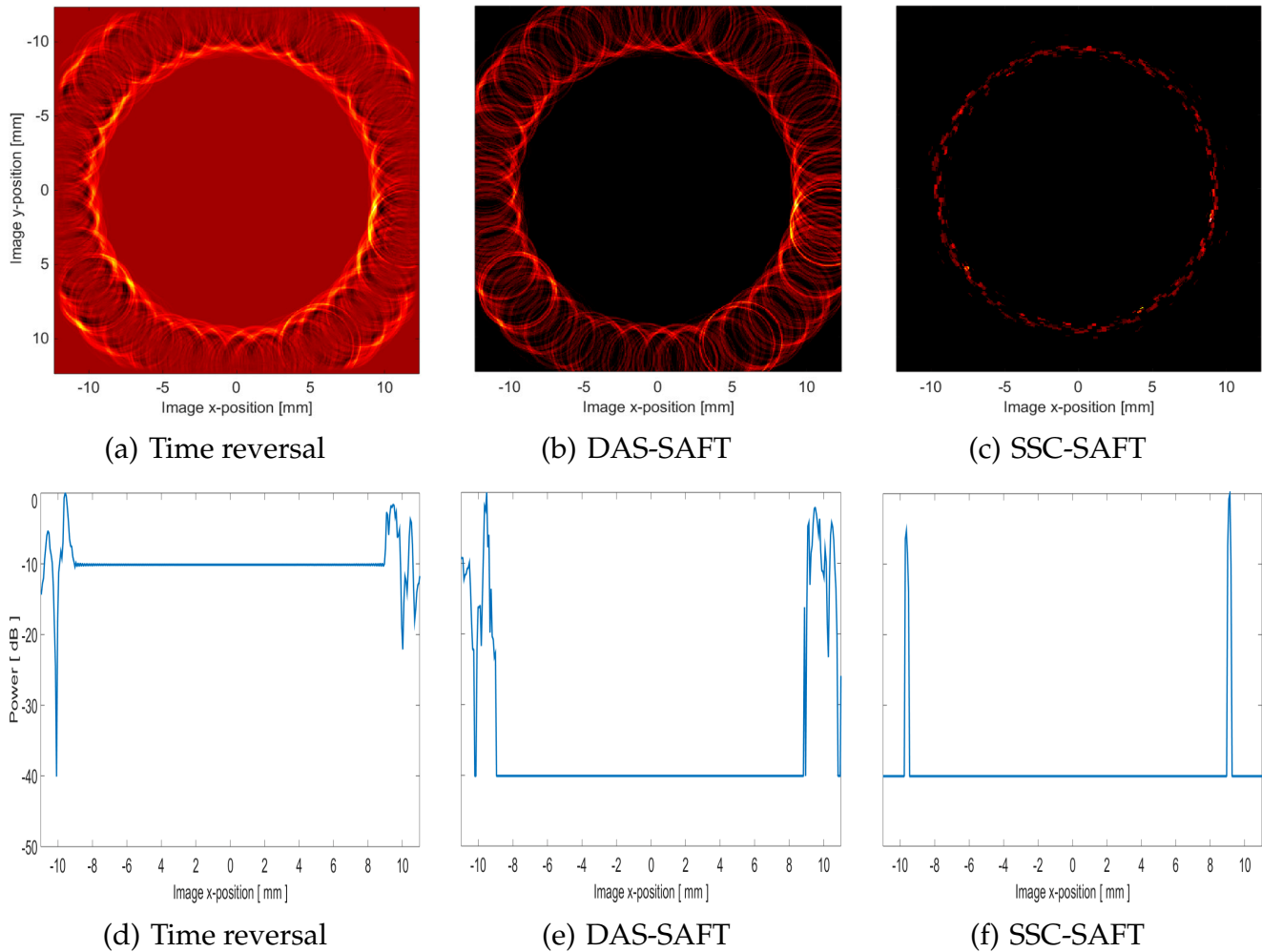(d) Time reversal　　　(e) DAS-SAFT　　　(f) SSC-SAFT

Figure 3.11: (a)-(c) Resulted images, after the signal thresholding and using the reconstruction method indicated, for the contiguous copper wires. (d)-(f) Lateral variation profiles of the intensity image, for the region at 0 mm of the image y-position and from -11 mm to $+11$ mm of the image x-position.

Quality parameter	Time reversal	DAS-SAFT	SSC-SAFT
Side-lobe level (dB)	-11.75, -3.73	-16.23, -4.26	–
FWHM (μm)	314	610	240
SNR (dB)	56.16	48.11	71.02
Processing time (s)	18.2	86.1	0.3

Table 3.2: Quantitative parameters of the intensity images obtained from the PA scanning of the contiguous copper wires. The side lobe levels and FWHM were estimated from the LVP. The SNR was calculated from the whole image.

the shape of the recovered object. The superposition of these artifacts results in a complex object that does not correspond to the actual shape of the sample. The

SSC-SAFT corrects this issue, removing the side-lobe artifacts and avoiding its superposition, providing a better reconstruction of the sample, noticing that the curvature of the illuminated region of the wires is recovered in the image resulting in a better definition of the sample studied.

3.3.4   Low SNR resolution: solid object of polylactic acid

The set of electrical signals acquired during the scanning is fundamental information to perform the image reconstruction, then, the quality of the electrical signals is a relevant characteristic of the entry information to recover the sample in an intensity image. The fundamental purpose of an image reconstruction method is to display in an intensity image the information contained in a set of electrical signals.

If the electrical signal has no information about a characteristic of the sample, the image will not either. If an electrical signal is distorted or noisy, the image will be too. The reverse direction of the reasoning is not necessarily ture, an inversion method can distort or lose some information of the electrical signals during the image formation. In this subsection, the recovering in the image of the information that are present in the electrical signal but with a low SNR will be studied. A solid decagrammic prism, made of polylactic acid (PLA), will be scanned. The sample was fabricated with a 3D printer and is shown in Fig. 3.12. The prism was illuminated in the perimeter of its transverse section, so the expected PA image is a ten-pointed star.
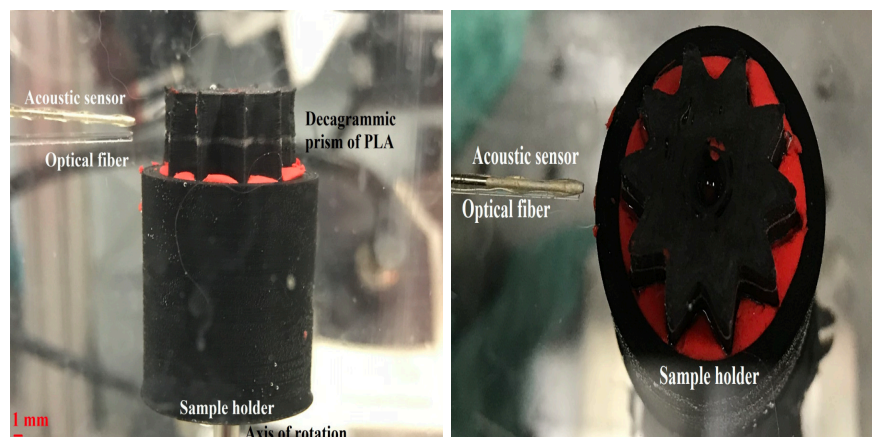

Figure 3.12: Photography of the sample scanned with the photoacoustic tomograph. The sample consists of a decagrammic prism of PLA.

The resulted sinogram of the electrical signals acquired is presented in the Fig.

3.13. Ten pair of regions with high amplitude can be observed, corresponding to the ten pair of peak-trough of the star, as well as the region that connect them, but with a considerably lower amplitude, and close to the intensity of the noise and background.
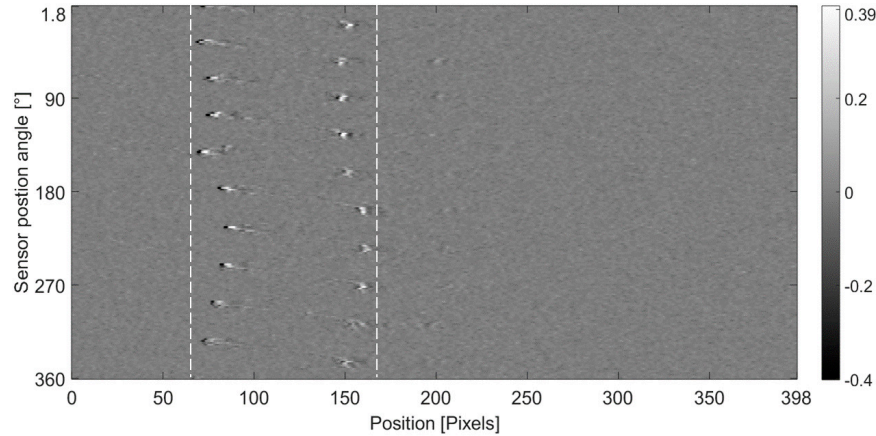

Figure 3.13: Sinogram of the electrical signals acquired during the scanning. The grayscale values correspond to the voltage amplitude of the signals. The ROI is enclosed between the doted lines.

The radius of the emulated circular sensor array is $r = 11.9$ mm, the computational grid was constructed with the following parameters: $x = 25.1$ mm, $Nx = 398$, and $\Delta x = 62$ μm. The Figs. 3.14 (a)-(c) presents PA images obtained without signal processing, the Figs. 3.14 (d)-(e) the resulted images with a threshold of $+0.08$ V.

Because of the geometry of the decagrammic prism and the directionality of the acoustic sensors, the peaks of the prism will generate a PA electrical signal of greater intensity than the region that connects each other, giving the impression of isolated targets. Then, the resulted time reversal and DAS-SAFT images are affected and distorted because of the side lobe artifacts and high sensitivity to noise and off-axis signals. Even with the understanding of the side lobe effects, the time reversal and DAS-SAFT images apparently retrieve a decagon-like pattern and ten isolated objects with a comet-tail sign, which does not correspond to the scanned sample. The objects in these images are blurry, and targets that generates a low signal-to-noise ratio could not appear in the final image. The SSC-SAFT shows to correct these issues, because of the segmented reconstruction, the main and high intensity side-lobe artifacts and comet-tail signs are completely removed and, considering the length of the effective sensing surface provokes regions with a lower SNR to be present in the final image, but barely defined, such as the information observed in the sinogram.

(a) Time reversal (b) DAS-SAFT (c) SSC-SAFT

(d) Time reversal - thresholding (e) DAS-SAFT - thresholding (f) SSC-SAFT - thresholding
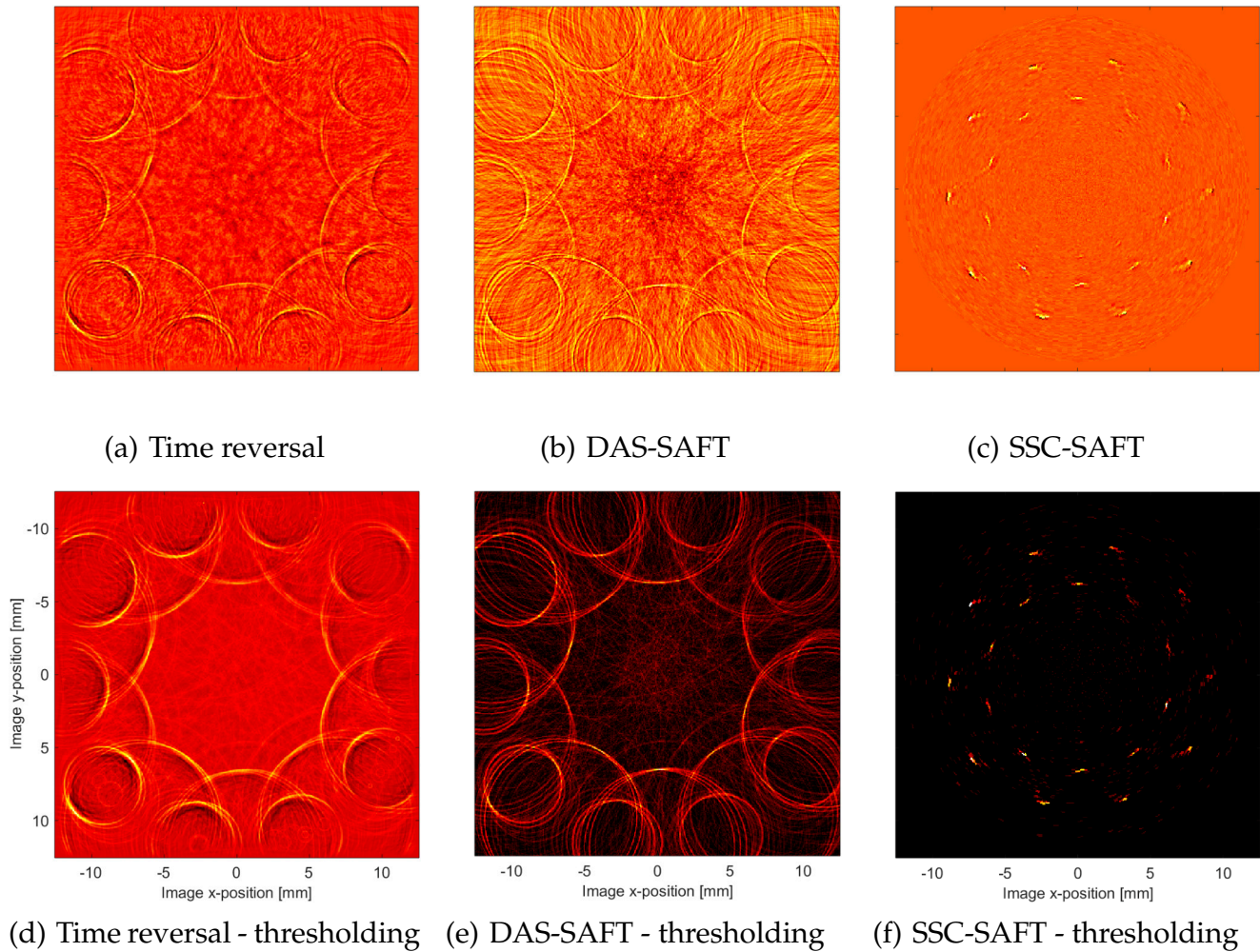
Figure 3.14: Resulted images using the reconstruction method indicated: (a)-(c) without signal processing, (d)-(e) after the signal thresholding.

For this sample, distinct from the previous ones, signal thresholding is not enough to show in the image the actual shape of the sample (a ten-pointed star) with a high contrast, as the region that connect peaks has an intensity close to that of the noise and the background, the thresholding removes both the noise and these regions, or leave the regions but poorly defined. Then a different signal processing is proposed.

3.3.4.1 Proposed digital signal processing protocol

Once the signals were filtered with the non-negative threshold, the high-frequency noise was removed with an Exponential Moving Average (EMA) filter, which is computed as:

$$A_n = \alpha S_n + (1 - \alpha)A_{n-1} \tag{3.7}$$

where S_n is the nth sample of the signal, A_n is the nth sample of the resulted filtered signal and α is a parameter, from 0 to 1, to modulate the strength of the filter, the lower the value of α, the higher the filtered frequencies. As the aim of this step of the signal processing is to increase the contrast between the objects in the image generated by signals with low SNR, once the high-frequency noise was removed, the set of electrical signals were normalized, so those waveforms in the signal with low amplitude (or SNR) were increased and compared with the waveforms with high SNR.

Then, a ROI is defined, and the same processing is performed to this section of the sinogram, the resulting two sets of filtered signals, those obtained after the EMA filtering and normalization of the initial set of signals and the filtered ROI, were added. Since there could be a remnant noise, but now with a lower amplitude compared with the electrical information of the waveform, a second thresholding is applied.

The aim of this electrical signal processing is to highlight a specific region of the electrical signals but without losing the possible information that is out of the ROI, removing the high-frequency noise and increasing the amplitude of the information with a low SNR, increasing the contrast of the reconstructed objects in the image. The two parameters needed to perform this signal processing protocol are α, from Eq. 3.7, and the value of the second threshold.

It is important to remark that the digital processing is performed on the electrical signals, not on the intensity images.

The parameters used to perform the electrical signal processing are 0.05 and 0.08, for α in Eq. 3.7 and for the second threshold respectively. The ROI was defined between the position 65 and 170 of the sinogram. The resulted images are presented in the Figs. 3.15 (a)-(c). As can be seen, even after the electrical signal processing, the time reversal and DAS-SAFT images are still distorted and with high side-lobe levels, demonstrating that these artifacts are not caused purely by the electrical noise nor by the low SNR. The SSC-SAFT shows to correct the issues, although the appearance of some isolated point-like objects that corresponds to the remnant noise in the signals that were not avoided with the second threshold, the image presents the ten-pointed star with higher contrast, recovering the lost sections before the signal processing.

To quantitatively compare the quality of the images, the lateral variation profiles was calculated for the region at a depth of -2.17 mm of the image y-position and from -8.00 mm to 8.00 mm of the image x-position, which corresponds to a pair of peaks of the ten-pointed star that is well defined in the three images, the resulted

(a) Time reversal

(b) DAS-SAFT

(c) SSC-SAFT

(d) Time reversal

(e) DAS-SAFT

(f) SSC-SAFT
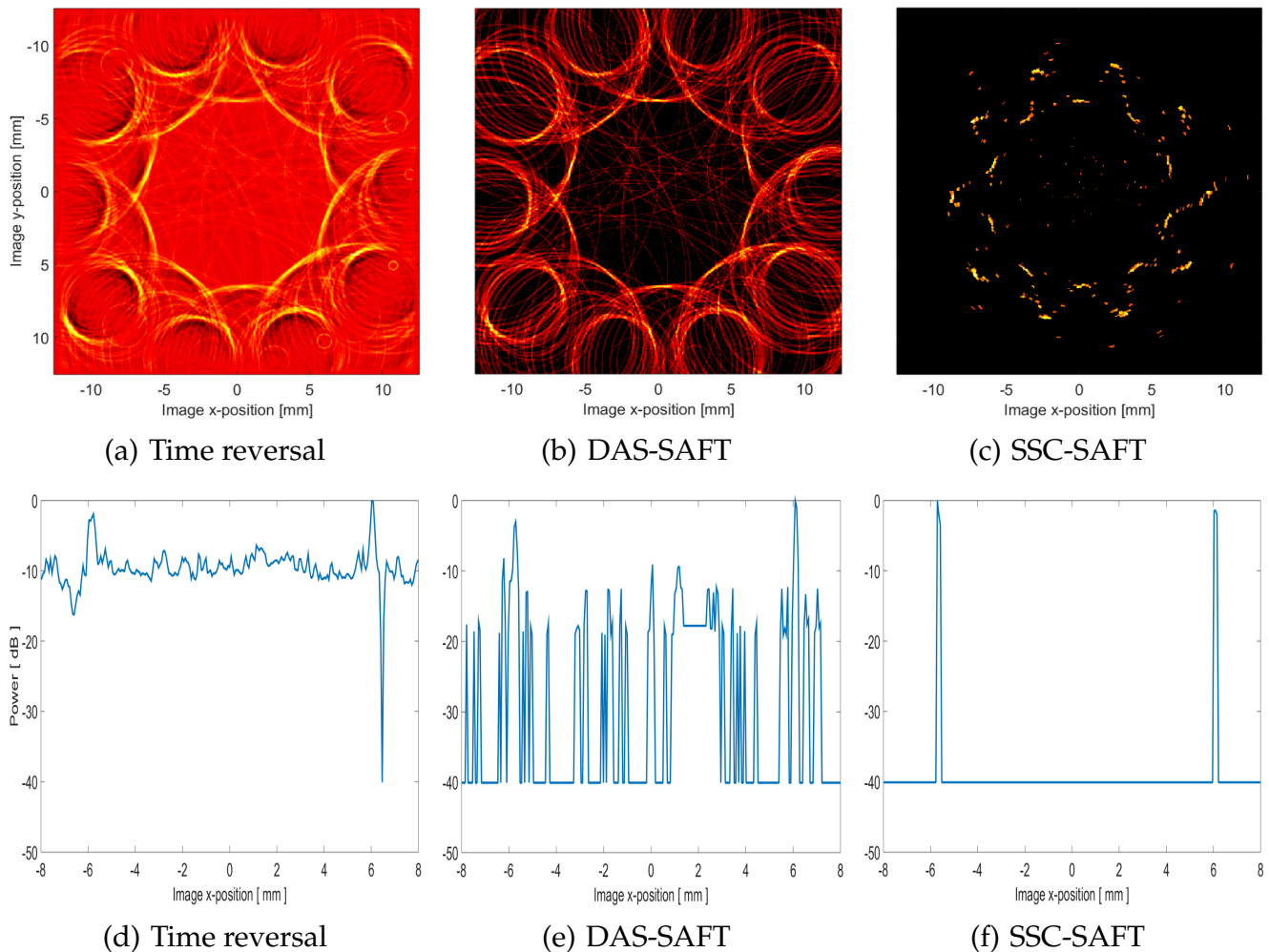
Figure 3.15: (a)-(c) Resulted images after the signal processing and using the reconstruction method indicated. (d)-(f) Lateral variation profiles calculated at a depth of 1.38 mm of the image y-position and from -6.00 mm to 6.00 mm of the image x-position.

profiles are presented in the Fig. 3.15 (d)-(f).

The estimated values of the side-lobe levels, the FWHM of the second peak of the region studied, the SNR, along with the total processing time for the images obtained are shown in the table 3.3.

The study of the lateral variation profiles shows that the SSC-SAFT image has a better quantitative quality, bringing a qualitative optimization of the of the image after the signal processing, recovering the regions of the scanned sample that has a low SNR in the electrical signals acquired.

Quality parameter	Time reversal	DAS-SAFT	SSC-SAFT
Side-lobe level (dB)	-8.58, -6.36	-18.60, -9.09	–
FWHM (μm)	355	282	188
SNR (dB)	50.69	39.31	54.02
Processing time (s)	19.4	92.6	0.3

Table 3.3: Quantitative parameters from the intensity images obtained. The side lobe levels and FWHM were estimated from the lateral variation profile. The SNR was calculated from the whole image.

3.4 *Ex vivo* tissue imaging

The capabilities of the SSC-SAFT have been demonstrated through a numerical calculation and experimental approaches using samples that are strongly optically absorbent with a specific geometric configuration. The biomedical imaging is the main objective of the PA imaging, and even though the biomedical diagnosis is not the purpose of this work, but the proposal of a reconstruction algorithm, the SSC-SAFT should be capable of recover some features of a biological tissue scanning. The image reconstruction achieved with the measurement technique and the proposed reconstruction method for two *ex vivo* tissues will be presented.

To accomplish the results presented in this section, a rat kidney and heart was scanned using the single-sensor measurement technique. The experiments were performed on male Sprague-Dawley rat aged three-week old, the animal was housed in a 12:12-hours light-dark cycle with food and water available *ad libitum*. The animal was deeply anesthetized, decapitated and the kidney and heart removed. This process was performed by Prof David Kline and Prof. Heather A. Dantzler (Department of Medical Pharmacology and Physiology, Department of Biomedical Science, and Dalton Cardiovascular Research Center, University of Missouri-Columbia). The experiments were performed following the National Institutes of Health Guide for the Care and Use of Laboratory Animals guidelines. Animal protocols were approved by the University of Missouri and Pennington Biomedical Research Center Animal Care and Use Committees.

In these experiments, a sensor made of PZT ceramic with a circular sensing surface of 1 mm ($A = 1$ mm in the notation described in Sec. 3.2.2) was used instead of the PVDF sensor. The PZT ceramic improves the signal quality compared with the PVDF when non-strongly optically absorbent materials are used, like the tissues studied. This change does not imply any modification nor implication in the algebra of the reconstruction method proposed and image reconstruction procedure. For the rat kidney, the purpose is to show how the capabilities of the

SSC-SAFT (artifact removal, spatial resolution, definition, and the recovering of information with low SNR) brings a better image of the tissue, compared with DAS-SAFT and time reversal, allowing a better interpretation of the result and a PA image that matches with the actual shape of the biological sample. For the rat heart, the objective is to present the result of a scanning in four different sections, a PA tomography, presenting the change on the recovered structure for the sample sections.

3.4.1 Rat kidney

The rat kidney was scanned using the PA tomograph, illuminating an upper cross section, near to the adipose tissue (fat), see Fig. 3.16. The resulted sinogram from the acquired electrical signals is presented in the Fig. 3.17. The PA information generated by the kidney is differentiable from the background, but with a low SNR. In addition, some patterns can be observed, like horizontal lines going from withe to black that spreads the entire sinogram, these are the high-frequency noise or artifacts, so the signal processing protocol, presented in the Sec. 3.3.4.1, is suitable for these measurements.
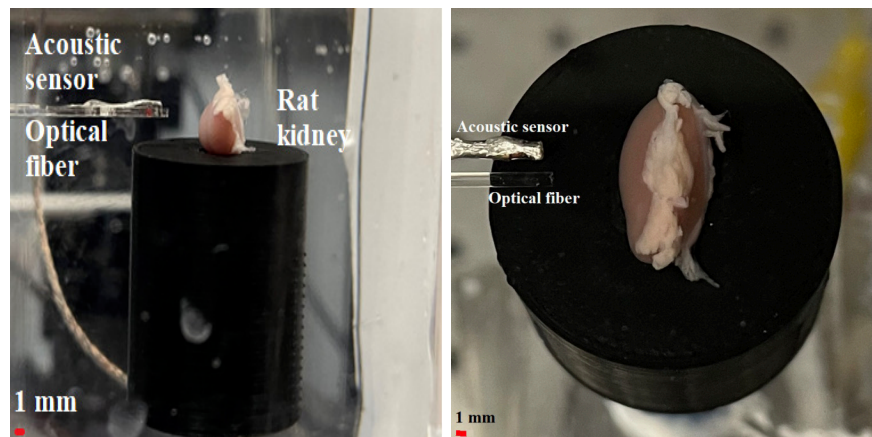

Figure 3.16: Photography of the sample scanned, an *ex vivo* rat kidney.

The distance between the sensing surface and the axis of rotation was $r = 8.3$ mm, the spatial length of the computational grid was set to $x = 17.5$ mm, with $Nx = 278$ nodes and a resulting pixel length of $\Delta x = 63$ μm. For the signal processing, the selected ROI was from the position 35 to 98 of the sinogram, the parameters used was $\alpha = 0.05$ and a threshold of $+0.15$ V. Because of the low SNR that can be observed in the sinogram, it is not appropriated to set the first threshold, as this removes only the low amplitude noise. The resulted PA images along with its LVP, studied from the region at a depth of -3.32 mm of the image y-
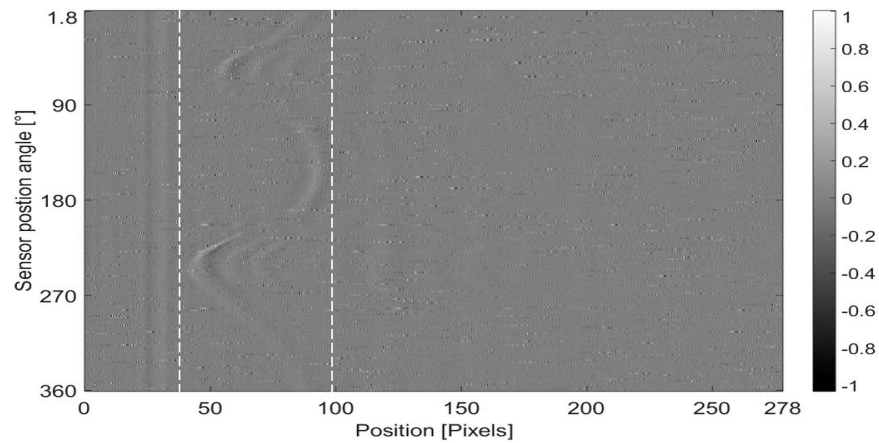
Figure 3.17: Sinogram of the electrical signals acquired during the scanning. The region studied is enclosed by the doted lines.

position and from -4.00 mm to -2.00 mm of the image x-position, are presented in the Figs. 3.18.

From the SSC-SAFT image, it can be noticed that not every sign of the noise could be removed, but a considerable high contrast and well-definition of the shape of the kidney are achieved. The quality parameters to compare the images are presented in the table 3.4, showing that the SSC-SAFT image has an improve on the FWHM, removing the artifacts, with a proper value of the SNR.

Quality parameter	Time reversal	DAS-SAFT	SSC-SAFT
Side-lobe level (dB)	-11.75, -4.15	-13.36, -4.19	–
FWHM (μm)	486	417	371
SNR (dB)	64.54	53.72	51.04
Processing time (s)	15.1	51.8	0.2

Table 3.4: Quantitative quality parameters from the intensity images obtained for the PA scanning of the rat kidney. The side lobe levels and FWHM were estimated from the lateral variation profile. The SNR was calculated from the whole image.

From the sinogram, furthermore the reverberation of the principal pattern, it is observed that there is no distinguishable information from inside the kidney, then the expected information in the images is the shape of the illuminated section of the tissue. The resulted images shows that the SSC-SAFT successfully recovers the kidney external structure, without side-lobe artifacts and with a high contrast despite the low SNR of the electrical signals, while the DAS-SAFT and time reversal images have high levels of side-lobe artifacts and a critical distortion of the

(a) Time reversal   (b) DAS-SAFT   (c) SSC-SAFT

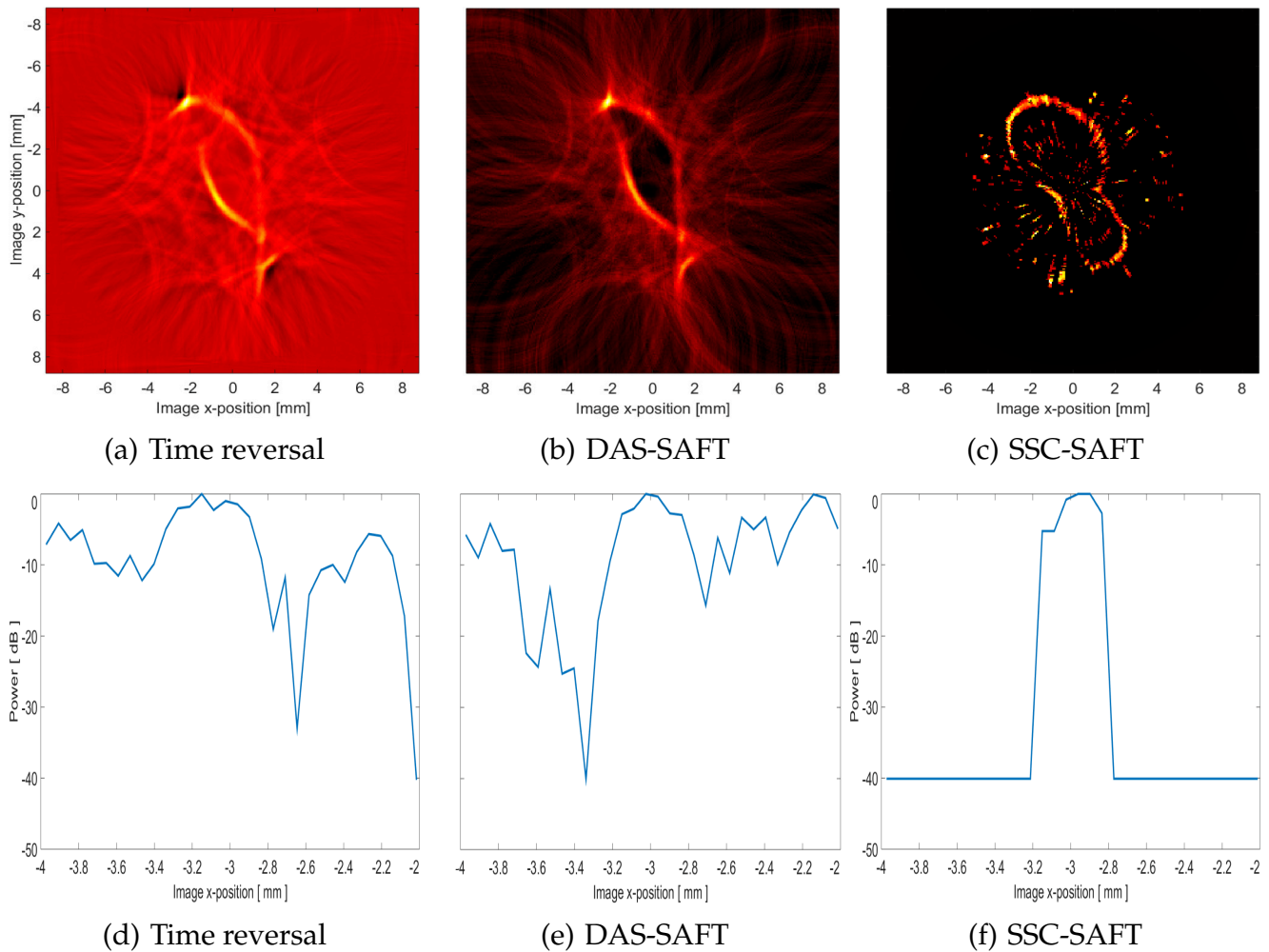(d) Time reversal   (e) DAS-SAFT   (f) SSC-SAFT

Figure 3.18: (a)-(c) Resulted images after the signal processing and using the reconstruction method indicated. (d)-(f) Lateral variation profiles from the region at a depth of -3.32 mm of the image y-position and from -4.00 mm to -2.00 mm of the image *x*-position.

recovered shape of the kidney. This is an example of what was discussed in the previous section: when the physical foundations of the measurement technique are not considered in a reconstruction method, it can deform the information of the electrical signals acquired, resulting in a reconstructed image that can be a misunderstood.

In order to compare the recovered shape of the kidney in the SSC-SAFT image, a superposition of the PA image with the photography of the kidney is presented in the Fig. 3.19. The noise artifacts external to the recovered structure was removed synthetically and the image rotated to match with the position of the kidney in the photography.
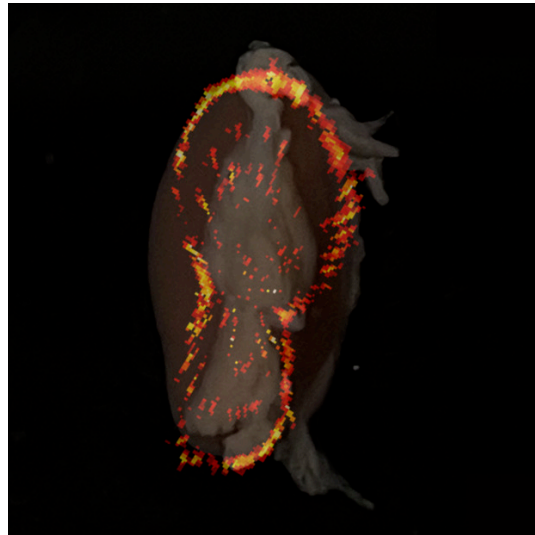
Figure 3.19: Superposition of the rat kidney photography and its SSC-SAFT image.

3.4.2   Photoacoustic tomography: rat heart

The rat heart was scanned using the PA tomograph with the single-sensor technique in four different sections of the sample separated by 1 mm, see Fig. 3.20.
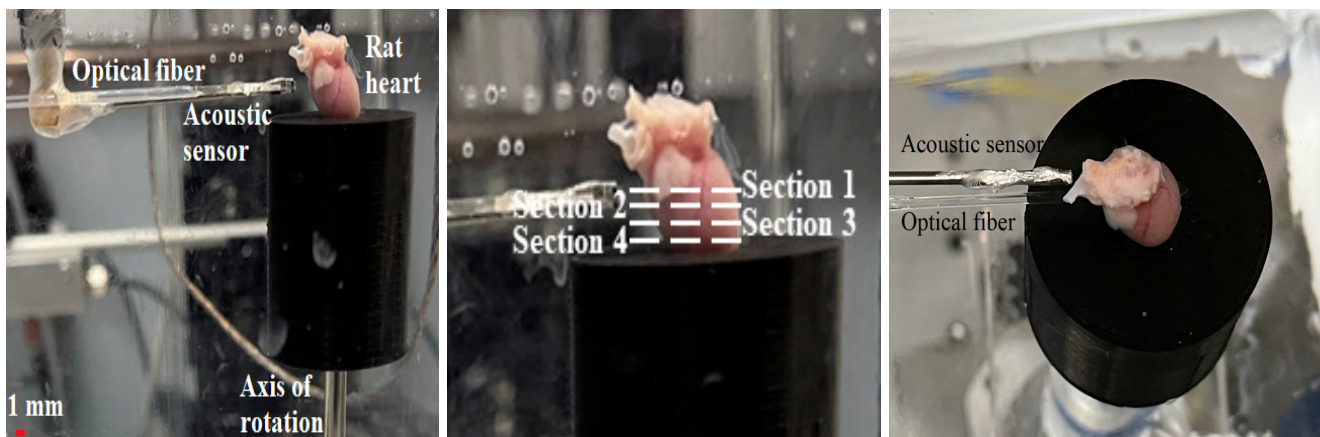
Figure 3.20: Photography of the rat heart scanned with the PA tomograph, indicating the four different sections studied.

The resulted sinograms for the four sections scanned are presented in the Fig. 3.21. To avoid crowding, the dynamic range bar to indicate the voltage value was omitted in the figures, as this is the same for the four cases, the color bar is the same that has been used in the previous sections, but with a voltage range from -1.20 V to $+1.20$ V. The patterns can be observed in all cases, but with a low SNR, so the discussed signal processing was performed for each set of electrical signals,

with the parameters: $\alpha = 0.05$, and a threshold of $+0.30$ V for sections 1 and 2, $+0.45$ V for the section 3, and $+0.50$ V for section 5. The studied ROI is presented between dotted lines.

(a) Section 1   (b) Section 2

(c) Section 3   (d) Section 4
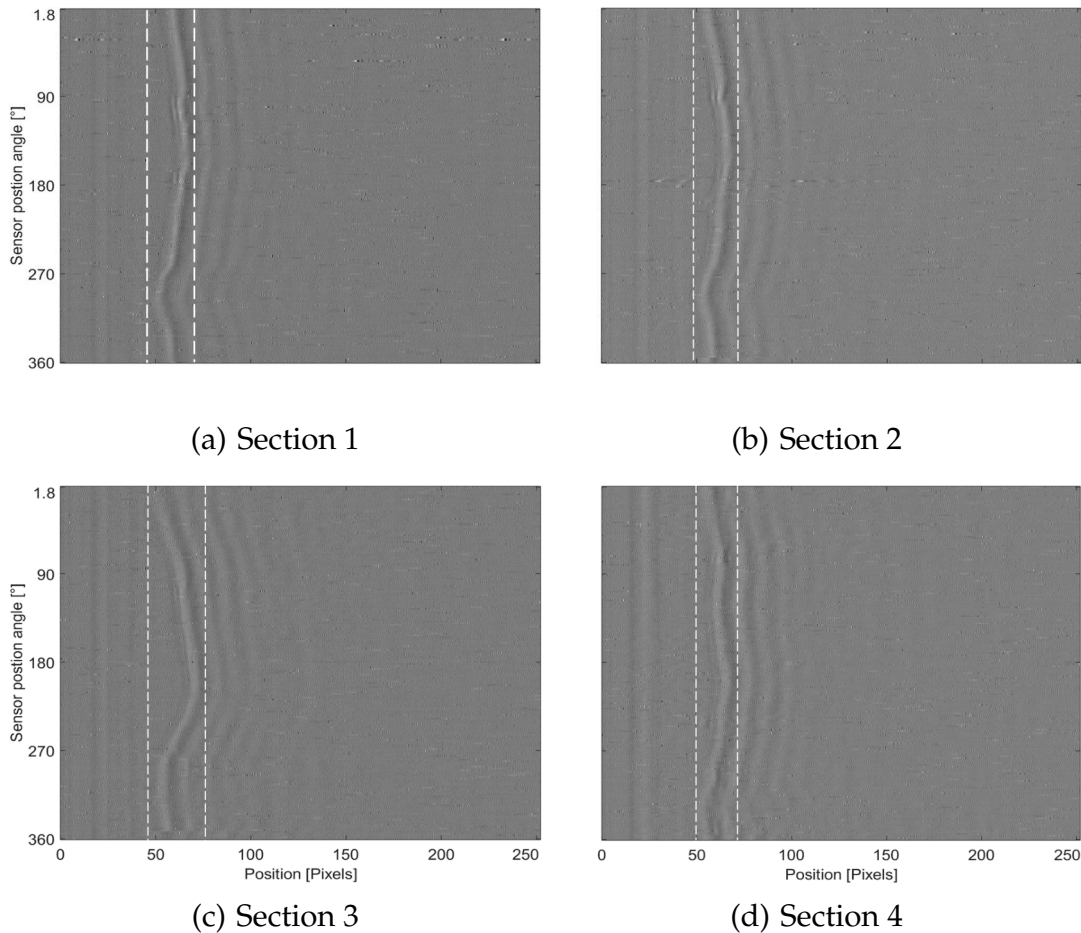
Figure 3.21: Sinograms of the PA scanning of the rat heart in the section indicated.

To perform the image reconstruction, the parameters used were $r = 7.5$ mm, $x = 15.9$ mm, $Nx = 252$, and $\Delta x = 63$ μm. The resulted PA images are presented in the Fig. 3.22. The PA images show the external structure of the rat heart, recovering the change in the shape of the heart for every region scanned. The contour of the reconstructed region of the heart is well defined despite there is a minimum sign of electrical noise in the images.

These studies demonstrate that the single-sensor measurement technique for PA tomography along with the proposed SSC-SAFT reconstruction method are suitable for the reconstruction of *ex vivo* biological tissues, allowing the study of the PA signals of this kind of samples and to explore the medical capabilities of the PA imaging techniques.

(a) Section 1

(b) Section 2

(c) Section 3

(d) Section 4

Figure 3.22: PA images recovered from the rat heart in the section indicated, after the electrical signal processing, and using the proposed SSC-SAFT reconstruction method.
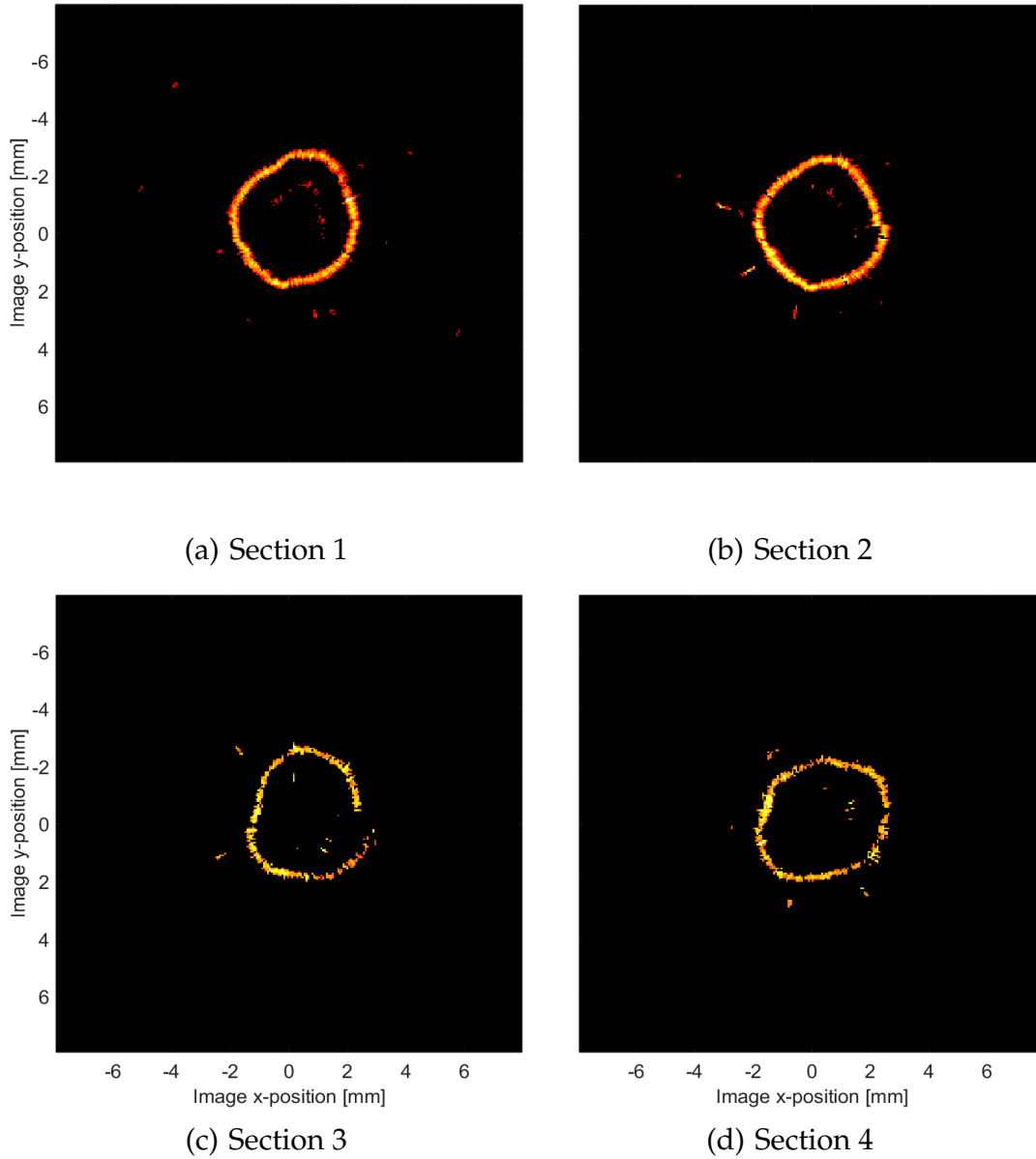
Chapter 4

Modeling of the photoacoustic signal

The SSC-SAFT has been proposed as a PA image reconstruction method and, as explained on Chapter 3 Sec. 3.2.2, it is independent of any physical model of the PA effect. The assumption of a constant medium sound speed, considered as the mean sound speed of the propagation medium, is the only physical constraint, and the calculation of the time delays as the quotient of an estimated distance and the medium sound speed is the only physical model involved. Nevertheless, because of the structure of the SSC-SAFT (Eq. (3.3)), the waveform of the PA electrical signal, and then the physical information it contains, will be inherited in its corresponding reconstruction line on the image.

The geometrical structure of the recovered targets in the PA images is a relevant characteristic that brings information on the shape of the studied samples. To bring a physical interpretation, moreover that the geometrical structure, a mathematical model of the physical characteristics of the PA electrical signal is needed.

In this chapter, a solution to the one-dimensional PA wave equation (Eq. (2.3) on Sec. 2.2) will be obtained for specific physical conditions. Then, the thermal and stress confinement conditions that lead to the wave equations will be analyzed and a thermally corrected solution will be proposed. Using the proposed solution, the sensor response will be considered, to obtain a model of the PA electrical signal that can be implemented to analyze the physical information of the PA images obtained through the SSC-SAFT.

4.1   One-dimensional solution of the photoacoustic wave equation

Starting with the PA wave equation, Eq. (2.3), a plane sample labeled s, with thickness L, and immerse on a non-optically absorbent fluid labeled f is considered. The stated problem is represented in the Fig. 4.1, following the scheme, the boundary value problem is defined by [51]:

$$\left(\frac{\partial^2}{\partial z^2} - \frac{1}{c_f^2}\frac{\partial^2}{\partial t^2}\right) P_B(z,t) = 0, \qquad\qquad z < 0; \qquad (4.1a)$$

$$\left(\frac{\partial^2}{\partial z^2} - \frac{1}{c_S^2}\frac{\partial^2}{\partial t^2}\right) P_S(z,t) = -\frac{\beta}{C_p}\frac{\partial H(z,t)}{\partial t}, \qquad 0 < z < L; \qquad (4.1b)$$

$$\left(\frac{\partial^2}{\partial z^2} - \frac{1}{c_f^2}\frac{\partial^2}{\partial t^2}\right) P_F(z,t) = 0, \qquad\qquad L < z; \qquad (4.1c)$$

with the boundary conditions:

$$P_B(z,t)\big|_{z=0} = P_S(z,t)\big|_{z=0}, \qquad (4.2a)$$

$$P_S(z,t)\big|_{z=L} = P_F(z,t)\big|_{z=L}, \qquad (4.2b)$$

$$\frac{1}{\rho_f}\frac{\partial}{\partial z}P_B(z,t)\bigg|_{z=0} = \frac{1}{\rho_s}\frac{\partial}{\partial z}P_S(z,t)\bigg|_{z=0}, \qquad (4.2c)$$

$$\frac{1}{\rho_s}\frac{\partial}{\partial z}P_S(z,t)\bigg|_{z=L} = \frac{1}{\rho_f}\frac{\partial}{\partial z}P_F(z,t)\bigg|_{z=L}. \qquad (4.2d)$$

The considered problem is a one-dimensional boundary value problem of the PA wave equation. The sub-indexes B and F are for backward and forward propagation modes, respectively, while S represents the pressure inside the sample.

4.1.1   Frequency domain solution

Because the expected solutions are a set of traveling waves, after a temporal Fourier transformation, the solutions for the spatial part of Eqs. (4.1) are [51]:

$$\hat{P}_B(z,\omega) = A_B(\omega)e^{j\omega z/c_f} + B_B(\omega)e^{-j\omega z/c_f}, \qquad z < 0; \quad (4.3a)$$

$$\hat{P}_S(z,\omega) = A_S(\omega)e^{j\omega z/c_S} + B_S(\omega)e^{-j\omega z/c_S} + \hat{P}_p(z,\omega), \quad 0 < z < L; \quad (4.3b)$$

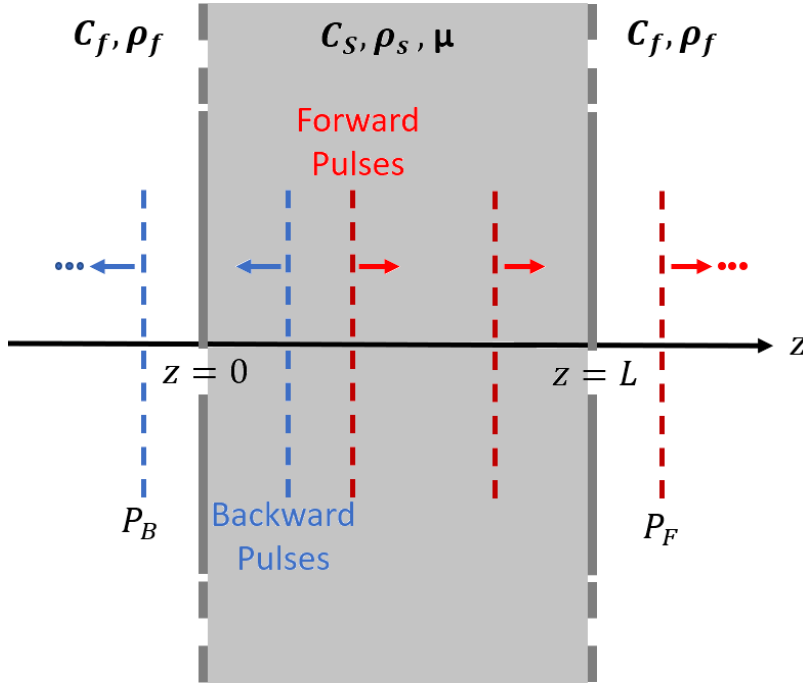$$\hat{P}_F(z,\omega) = A_F(\omega)e^{j\omega z/c_f} + B_F(\omega)e^{-j\omega z/c_f}, \qquad L < z; \quad (4.3c)$$

Figure 4.1: Schematic representation of the configuration studied. The sample is illuminated on the face located at $z = 0$.

The PA effect is a non-contact measurable technique, then the variables of experimental interest are given by (4.3a) and (4.3c), thus the Eq. (4.3b) will not be taken into account in the followed discussion. It is also assumed that the studied sample is the only source of PA waves, therefore, for $z < 0$ the considered solution is a left-traveling wave, and right-traveling for $z > 0$, which leads to $B_B = 0$ and $A_F = 0$. The Fourier transformation of the set of boundary conditions (4.2) leads into a system of equations that brings the information of the remaining ω-dependent functions A_B and B_F, obtaining:

$$A_B(\omega) = \overline{T}\frac{P_0}{2}\left(\frac{\overline{Y} - RYe^{-2j\omega\tau}}{1 - R^2e^{-2j\omega\tau}}\right)\hat{\theta}(\omega) \tag{4.4a}$$

$$B_F(\omega) = \overline{T}\frac{P_0}{2}\left(\frac{Y - R\overline{Y}}{1 - R^2e^{-2j\omega\tau}}\right)e^{-jk_f\left[c_f\tau - L\right]}\hat{\theta}(\omega), \tag{4.4b}$$

where $P_0 = \Gamma\mu I_0$, Γ is known as the Grüneisen parameter and is defined as $\Gamma \equiv c_S^2\beta/C_p$, $\hat{\theta}(\omega)$ is the Fourier transform of the temporal laser profile $\theta(t)$, $\tau = L/c_S$ is the single-trip time-of-flight of the acoustic wave in the slab, $\omega_{ac} \equiv \mu c_S$ is the characteristic ultrasonic frequency of the PA wave, with μ the optical absorption coefficient. The acoustic reflectivity coefficient for fluid and sample is $R \equiv \left(Z_s - Z_f\right)/\left(Z_s + Z_f\right)$ with $\left(\overline{T} = 1 - R\right)$, where $Z_l \equiv c_l\rho_l$ with $l = \{f,s\}$ for fluid and sample respectively. $Y \equiv \left[1 - e^{-(\omega_{ac} - j\omega)\tau}\right]/(\omega_{ac} - j\omega)$ and $\overline{Y}$ its

complex conjugate.

Inserting the founded coefficients (Eqs. (4.4)) in the Eqs. (4.3), and using the mathematical equality $\left(1 - R^2 e^{-j2\omega\tau}\right)^{-1} = \sum_{n=0}^{\infty} R^{2n} e^{-j2n\omega\tau}$, the solutions to the 1D PA wave equation in the temporal Fourier domain are:

$$\hat{P}_B(z,\omega) = \overline{T}\frac{P_0}{2}\sum_{n=0}^{\infty} R^{2n} \left\{ \left[\frac{e^{j\omega\left(\frac{z}{c_f}-2n\tau\right)}}{\omega_{ac} + j\omega} - e^{-\omega_{ac}\tau}\frac{e^{j\omega\left[\frac{z}{c_f}-(2n+1)\tau\right]}}{\omega_{ac} + j\omega} \right] \right.$$
$$\left. - R\left[\frac{e^{j\omega\left[\frac{z}{c_f}-2(n+1)\tau\right]}}{\omega_{ac} - j\omega} - e^{-\omega_{ac}\tau}\frac{e^{j\omega\left[\frac{z}{c_f}-(2n+1)\tau\right]}}{\omega_{ac} - j\omega} \right] \right\} \hat{\theta}(\omega), \qquad z \leq 0; \tag{4.5a}$$

$$\hat{P}_F(z,\omega) = \overline{T}\frac{P_0}{2}\sum_{n=0}^{\infty} R^{2n} \left\{ \left[\frac{e^{-j\omega\left[\frac{z-L}{c_f}+(2n+1)\tau\right]}}{\omega_{ac} - j\omega} - e^{-\omega_{ac}\tau}\frac{e^{-j\omega\left[\frac{z-L}{c_f}+2n\tau\right]}}{\omega_{ac} - j\omega} \right] \right.$$
$$\left. - R\left[\frac{e^{-j\omega\left[\frac{z-L}{c_f}+(2n+1)\tau\right]}}{\omega_{ac} + j\omega} - e^{-\omega_{ac}\tau}\frac{e^{-j\omega\left[\frac{z-L}{c_f}+2(n+1)\tau\right]}}{\omega_{ac} + j\omega} \right] \right\} \hat{\theta}(\omega), \quad z \geq L. \tag{4.5b}$$

4.1.2 Time domain solutions

The time-domain solutions will be founded as the inverse Fourier transform of the Eqs. (4.5). When the laser temporal profile is defined as an impulse response, the Fourier transform of the profile is $\hat{\theta}(\omega) = 1/\sqrt{2\pi}$. The resulted time-domain solutions are:

$$P_{X\delta}(\tau_B) = \sum_{n=0}^{\infty} \left\{ P_{X\delta}^{[2n\tau]}(\tau_X) - RP_X^{[(2n+1)\tau]}(\tau_X) \right\}, \tag{4.6}$$

with

$$P_{B\delta}(\tau_B) = \sum_{n=0}^{\infty} R^{2n} \left\{ P_{B\delta}^{[-2n\tau]}(\tau_B) - Re^{-2\tau/\tau_{ac}} P_B^{[+2n\tau]}(\tau_B) \right\}, \qquad z \leq 0; \tag{4.7a}$$

$$P_{F\delta}(\tau_F) = \sum_{n=0}^{\infty} \left\{ P_{F\delta}^{[2n\tau]}(\tau_F) - RP_F^{[(2n+1)\tau]}(\tau_F) \right\}, \qquad z \geq L; \tag{4.7b}$$

where $X = B$ (Backward) or F (Forward) for $z \leq 0$ or $z \geq L$, respectively. And where

$$P_{B\delta}^{[2n\tau]}(\tau_B) = \overline{T}\frac{P_0}{2}R^{2n}e^{-(\tau_B-2n\tau)/\tau_{ac}}\Pi\left[\frac{\tau_B - \left(2n + \frac{1}{2}\right)\tau}{\tau}\right]; \qquad (4.8a)$$

$$P_{B\delta}^{[(2n+1)\tau]}(\tau_B) = \overline{T}\frac{P_0}{2}R^{2n}e^{[\tau_B-2(n+1)\tau]/\tau_{ac}}\Pi\left[\frac{\tau_B - \left[(2n+1) + \frac{1}{2}\right]\tau}{\tau}\right]; \qquad (4.8b)$$

$$P_{F\delta}^{[2n\tau]}(\tau_F) = \overline{T}\frac{P_0}{2}R^{2n}e^{-\tau/\tau_{ac}}e^{(\tau_F-2n\tau)/\tau_{ac}}\Pi\left[\frac{\tau_F - \left(2n + \frac{1}{2}\right)\tau}{\tau}\right]; \qquad (4.8c)$$

$$P_{F\delta}^{[(2n+1)\tau]}(\tau_F) = \overline{T}\frac{P_0}{2}R^{2n}e^{-[\tau_F-(2n+1)\tau]/\tau_{ac}}\Pi\left[\frac{\tau_F - \left((2n+1) + \frac{1}{2}\right)\tau}{\tau}\right]; \qquad (4.8d)$$

with the definitions: $\tau_{ac} \equiv 1/\omega_{ac}$, $\tau_B \equiv t + z/c_f$, $\tau_F \equiv t - (z - L)/c_f$, and

$$\Pi\left[\frac{\tau_{B,F} - \left((2n + m) + \frac{1}{2}\right)\tau}{\tau}\right]$$

with $m = 0, 1$, being the rectangular function centered at $\tau_{B,F} = [(2n + m) + 1/2]\tau$ and of width τ.

As discussed, the time-domain impulse response is a correct approximation when the stress confinement condition is satisfied. Nevertheless, the pulsed beam of the actual laser devices is modeled with a Gaussian temporal profile of width $1/e$ equal to $\tau_p/2$,

$$\theta(t) = \left(2/\tau_p\sqrt{\pi}\right)e^{-(2t/\tau_p)^2}.$$

To obtain the solution of the 1D boundary value problem considering the Gaussian temporal profile, the time-domain impulse response in convolution with the temporal profile will be used:

$$P_k\left(\tau_{B,F}\right) = P_{k\delta} * \theta\left(\tau_{B,F}\right) = \int_{-\infty}^{+\infty}\theta(t)P_{k\delta}\left(\tau_{B,F} - t\right)dt,$$

Then, for the described pulsed beam, the solutions are:

$$P_B(\tau_B) = \sum_{n=0}^{\infty} R^{2n} \left[P_B^{[2n\tau]}(\tau_B) - RP_B^{[(2n+2)\tau]}(\tau_B) \right], \tag{4.9a}$$

$$P_F(\tau_F) = e^{-\frac{\tau}{\tau_{ac}}} \sum_{n=0}^{\infty} R^{2n} \left[P_F^{[2n\tau]}(\tau_F) - RP_F^{[(2n+2)\tau]}(\tau_F) \right], \tag{4.9b}$$

where

$$P_B^{[2n\tau]}(\tau_B) = \bar{T} \frac{P_0}{2} e^{-\left(\frac{\tau_p}{4\tau_{ac}}\right)^2} e^{-\frac{\tau_B - \tau_B^{2n}}{\tau_{ac}}} \frac{1}{2} \left[\mathrm{erf} \left(\frac{\tau_B - \tau_B^{2n}}{\frac{\tau_p}{2}} \right) - \mathrm{erf} \left(\frac{\tau_B - \tau_B^{2n} - \tau}{\frac{\tau_p}{2}} \right) \right], \tag{4.10a}$$

$$P_B^{[(2n+2)\tau]}(\tau_B) = \bar{T} \frac{P_0}{2} e^{-\left(\frac{\tau_p}{4\tau_{ac}}\right)^2} e^{\frac{\tau_B - \tau_B^{2n+2}}{\tau_{ac}}} \frac{1}{2} \left[\mathrm{erf} \left(\frac{\tau_B - \tau_B^{2n+1}}{\frac{\tau_p}{2}} \right) - \mathrm{erf} \left(\frac{\tau_B - \tau_B^{2n+1} - \tau}{\frac{\tau_p}{2}} \right) \right], \tag{4.10b}$$

$$P_F^{[2n\tau]}(\tau_F) = \bar{T} \frac{P_0}{2} e^{-\left(\frac{\tau_p}{4\tau_{ac}}\right)^2} e^{\frac{\tau_F - \tau_F^{2n}}{\tau_{ac}}} \frac{1}{2} \left[\mathrm{erf} \left(\frac{\tau_F - \tau_F^{2n}}{\frac{\tau_p}{2}} \right) - \mathrm{erf} \left(\frac{\tau_F - \tau_F^{2n} - \tau}{\frac{\tau_p}{2}} \right) \right], \tag{4.10c}$$

$$P_F^{[(2n+2)\tau]}(\tau_F) = \bar{T} \frac{P_0}{2} e^{-\left(\frac{\tau_p}{4\tau_{ac}}\right)^2} e^{-\frac{\tau_F - \tau_F^{2n+2}}{\tau_{ac}}} \frac{1}{2} \left[\mathrm{erf} \left(\frac{\tau_F - \tau_F^{2n+1}}{\frac{\tau_p}{2}} \right) - \mathrm{erf} \left(\frac{\tau_F - \tau_F^{2n+1} - \tau}{\frac{\tau_p}{2}} \right) \right], \tag{4.10d}$$

and $\tau_{ac} \equiv 1/\omega_{ac}$ is the characteristic acoustic time, $\tau_B^{2n} = 2n\tau + \tau_p^2/8\tau_{ac}$, $\tau_B^{2n+m} = (2n+m)\tau - \tau_p^2/8\tau_{ac}$, $\tau_F^{2n} = 2n\tau - \tau_p^2/8\tau_{ac}$ and $\tau_F^{2n+m} = (2n+m)\tau + \tau_p^2/8\tau_{ac}$ with $m = 1, 2$.

4.2 Thermally corrected solutions of the photoacoustic wave equation

In the solutions (4.10), the difference between the error functions behave as a smoothed rectangular function, a quasi-rectangular function, then, the Eqs. (4.8) and (4.10) are the product of an exponential term and a rectangular function. In both structures, the exponential term models the electromagnetic-to-mechanical energy conversion, with a rise time related to the light penetration depth, the rectangular (or quasi-rectangular) function could be interpreted as the space-temporal confinement of this energy. Then, the founded solutions will be non-zero just

when the exponential and rectangular (or quasi-rectangular) rise times are coupled.

For the case of the impulse-response, Eqs. (4.7), the rise time of the rectangular function is zero, so the coupling with its corresponding exponential term will always be achieved. For the case of the finite Gaussian pulse, the rise time of the quasi-rectangular function is $\tau_p/2$, and then, the solution will be non-zero just for energy conversion rise times compared to that.

Under this reasoning, for strongly optically-absorbent materials, the predicted PA pressure will be equal to zero, while the PA signal for this kind of materials (e.g. metals) has been observed, which is an inconsistency in the solution to the 1D boundary-value problem of the PA wave equation.

To find the potential source of discrepancy between the physical model predictions and the experimental observations, it is important to remark that a fundamental assumption to obtain the PA wave equation is the thermal confinement condition, that requires the laser pulse time to be shorter than the heat diffusion time, so the heat conduction can be neglected. Even though the transformation process from optical to thermal energy is a very fast phenomenon, the heat can spread a distance larger than $1/\mu$ during the illumination time, unsatisfying the thermal confinement condition and then the accuracy of the PA wave equation.

An approach to overcome the contradiction generated by the breach of the thermal confinement condition could be to solve the coupled Eqs. (2.1) and (2.2), actually removing the need of a thermal confinement assumption. However, to the best of my knowledge, this problem has not an analytical solution. In order to have a solution, the next hypothesis is proposed: *It is assumed that during the time τ_p, heat travels a characteristic thermal length $l_{th} = 4\sqrt{\chi\tau_p}$ (thermal source), in consequence, the effective PA source is $l_{eff} = 4\sqrt{\chi\tau_p} + 1/\mu$ (thermal plus optical source), then, the characteristic acoustic time becomes*

$$\tau_{ac} \rightarrow \tau_{eff} \equiv \frac{l_{eff}}{c_S} = \left(1 + 4\mu\sqrt{\chi\tau_p}\right)\tau_{ac}. \tag{4.11}$$

The proposed hypothesis of the use of τ_{eff} instead of τ_{ac} implies the use of $\omega_{eff} = 1/\tau_{eff}$ instead of ω_{ac} in the Eqs. (4.9).

4.3   Modeling of the sensor and oscilloscope contributions on the electrical photoacoustic signal

The Eqs. (4.9) along with the proposed thermal correction, Eq. (4.11), bring a mathematical description of the waveform of the laser-induced ultrasound through the PA effect. To have a description of the acquired electrical signal related to the detected ultrasound wave, it is necessary to consider the sensor response and the connection device.

The sensing material of the acoustic detector is a piezoelectric (PVDF or PZT) foil, when the PA pressure hits on the piezoelectric surface, it generates an electric charge on the foil that flows from it to the oscilloscope along a cable. The electrical circuit that describes this phenomenon is a parallel RC circuit, Fig. 4.2, with a time-varying charge Q_0 generated by the piezoelectric foil, parallel connected through a cable to a resistance R_e and a capacitance C, which are related to the input impedance of the oscilloscope. The electrical circuit generates an electric potential difference $U(t)$, that describes the acquired electrical signal.
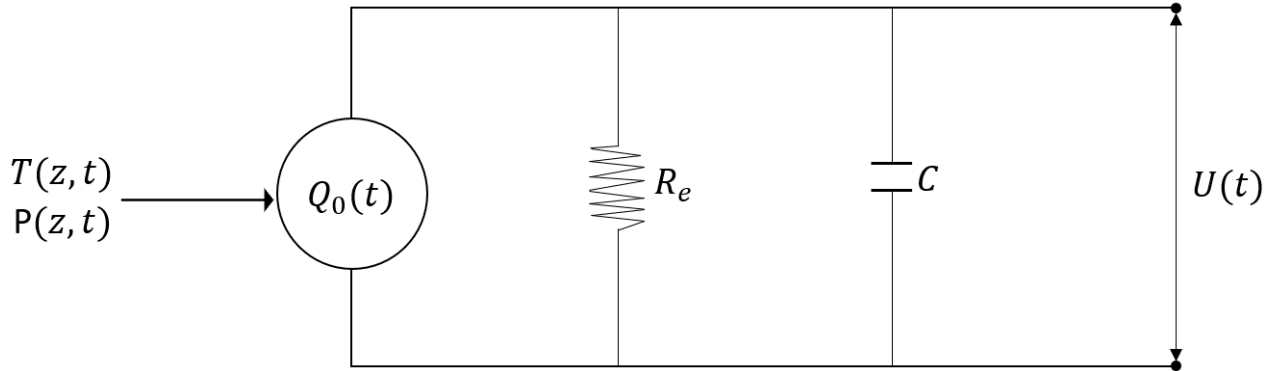
Figure 4.2: Equivalent electrical circuit that describes the PA electrical signal acquisition. The PA pressure generates a charge Q_0 on the piezoelectric foil that is connected to an oscilloscope of input impedance dependent on a resistance R_e and a capacitance C.

The differential equation for the charge is:

$$R_e C \frac{dQ}{dt} + Q(t) = Q_0(t) \tag{4.12}$$

as the time varying charge is generated by the PA pressure $P(z,t)$, it is modeled as [52]:

$$Q_0(t) = \frac{e_{33}A}{d} \int_0^d P(z,t)dz = e_{33}A\overline{P}(t), \qquad (4.13)$$

where A is the active area of the transducer, e_{33} is the piezoelectric stress constant, d is the thickness of the foil and $\overline{P}(t)$ is the mean stress inside it.

Then, the detected electric potential difference will be derived from the solution to the differential Eq. (4.12). In the frequency domain, this solution can be calculated as $\hat{Q}(\omega) = \hat{F}(\omega)\overline{P}(\omega)$ [53], where $\hat{F}(\omega)$ is the transfer function of the circuit, and was calculated from the Eq. (4.12), obtaining:

$$\hat{F}(\omega) = \frac{e_{33}A}{\sqrt{2\pi}} \frac{1}{1 + j\omega R_e C}. \qquad (4.14)$$

The spatial mean values $\overline{P}(\omega)$, for both Backward and forward PA pressure, can be calculated considering a detection position z_X on the Eqs. (4.5) and integrating over the piezoelectric thickness d, resulting in:

$$\overline{P}_X(z_X, \omega) = \frac{1}{j\omega t_d} \left[\hat{P}_X(z_X - d, \omega) - \hat{P}_X(z_X, \omega) \right] = \frac{1}{j\omega t_d} \left(1 - e^{-j\omega t_d} \right) \hat{P}_X(z_X, \omega)$$

$$(4.15)$$

where $X = B$ (Backward) or F (Forward), $t_d = d/c_{piezo}$, being c_{piezo} the sound speed in the piezoelectric, z_X is the position where the PA wave impinge the sensor and, P_X is given by Eq. (4.5a) for $X = B$ and (4.5b) for $X = F$.

Obtained the structure of $\hat{F}(\omega)$ and $\overline{P}(\omega)$, the charge is calculated as $\hat{Q}(\omega) = \hat{F}(\omega)\overline{P}(\omega)$, and the potential difference as $\hat{U}(\omega) = j\omega R_e \hat{Q}(\omega)$. Then, from Eqs. (4.9a) and (4.9b) in the time domain, $U_X(t)$ can be expressed as

$$U_X(t) = \frac{R_e}{t_d} I(t) * \left[P_X(\tau_X - t_d) - P_X(\tau_X) \right],$$

where $I(t)$ is the impulse response of the sensor, * indicates the convolution operation, and P_X are given by Eqs. (4.9). Remarking that the multiplication in the Fourier domain is transformed into a convolution in the time domain.

Considering that the RC electric circuit has a low impedance, then, the relation $\omega R_e C \ll 1$ is satisfied and the transfer function (Eq. (4.14)) can be approximated as

$$\hat{F}(\omega) \approx e_{33}A/\sqrt{2\pi}$$

which implies that the sensor impulse response can be approximated as a Dirac Delta distribution, and the convolution process results in:

$$U_X(t) \approx \frac{R_e}{t_d} \left[P_X(\tau_X - t_d) - P_X(\tau_X) \right]. \qquad (4.16)$$

Which is the desired model for the PA electrical signal in the time domain.

4.4 Numerical and experimental approach

To evaluate the accuracy of the founded solutions, a numerical implementation of the thermally corrected solutions (Eqs. (4.9)) and the model of the PA electrical signal (Eq. (4.16)) was performed and compared with the electrical signals acquired through an experimental observation.

An aluminum slab, which is a strong optical absorber, immersed in water, was used to perform the experiment. The values of the physical properties for aluminum (sample, s) and water (fluid, f) used were: ultrasound speed $c_s = 6.32 \times 10^3$ m/s and $c_f = 1.498 \times 10^3$ m/s; mass density $\rho_s = 2.7 \times 10^3$ kg/m³ and $\rho_f = 1 \times 10^3$ kg/m³; optical absorption coefficient $\mu = 1.4399 \times 10^8$ 1/m; specific heat capacity at constant pressure $C_P = 9 \times 10^2$ J/kgK; volumetric thermal expansion coefficient $\beta = 6.9 \times 10^{-5}$ 1/K; and a thermal diffusivity $\chi = 9.7 \times 10^{-5}$ m²/s. This leads to a characteristic specific acoustic impedance mismatch between the strong absorbing optical plane sample and its surrounding fluid of $Z_s = 1.706 \times 10^7$ Kg/m² s and $Z_f = 1.498 \times 10^6$ Kg/m² s. For the sensor, it was assumed a sound speed of 2.2×10^3 m/s and a thickness of 100 μm.

To acquire the electrical signals, the experimental setup involved is shown in the Figs. 4.3(a) and 4.3(b) for the case of the forward and backward propagation mode respectively.The incidence angle in backward mode was less than 2°. The laser used to illuminate the sample was a Nd: YAG laser coupled to an optical parametric oscillator system tuned in at 715 nm. The laser fluence per pulse was set at $I_0 = 30$ mJ/cm² and a beam spot diameter of 12 mm. In the near field, the spatial beam profile can be approximated as a flat-top beam, with a Gaussian temporal profile with a pulse duration of $\tau_p = 8 \times 10^{-9}$ s and a repetition rate of 10 Hz.

A 50 mm-diameter metallic slab was machined from a 99.999 % pure aluminum rod with 2.921 mm of thickness. The sensor used was a 40 μm needle hydrophone, and the pre-amplified electrical signal was acquired with a 500 MHz digital oscilloscope at a sampling rate of 5 GS/s, triggered by the laser control system. In

order to reduce the random or uncorrelated noise, 32 consecutive measurements were averaged.
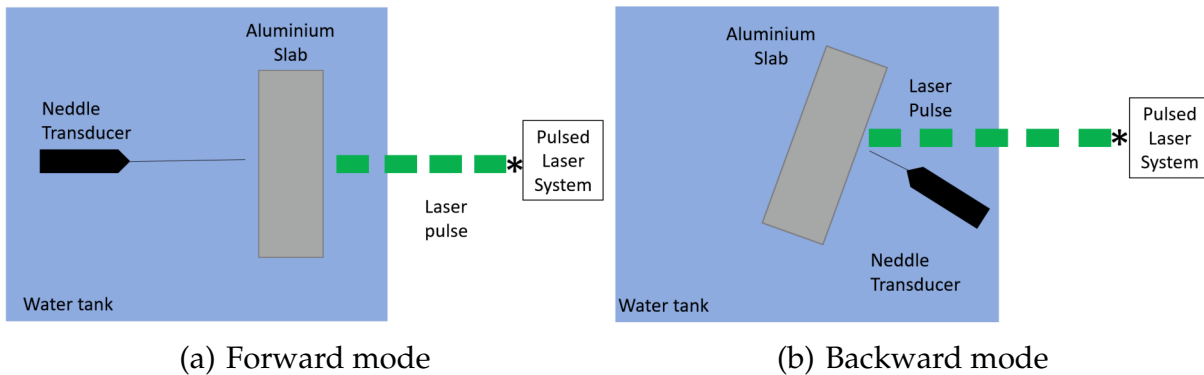

(a) Forward mode   (b) Backward mode

Figure 4.3: Experimental setup to generate PA wave in aluminium slab.

The averaged time-domain PA signals are show in the figure 4.4 along with the thermally corrected solutions, Eqs. (4.9), for the backward and forward propagation mode. In comparison with the description of the impulse-response solution discussed in the Sec. 4.2, the thermally corrected solutions are different from zero for the case of a strongly optically-absorbent material like the aluminum slab, solving the discussed discrepancy. The main agreement between the numerical solution and the electrical signal is with the time of flight of the different peaks. The theoretical prediction of the attenuation of the reflections, $Tp_0R^{2n}/2$ and $-Tp_0R^{2n+1}/2$ in Eqs. (4.9), is not observed in the electrical signals acquired. This is effect is because the PA electrical signal is affected by the sensor bandwidth and the acoustical reflections inside of it.

The Fig. 4.5(a) and 4.5(b) shows a comparison between the averaged time-domain PA electrical signals and its corresponding numerical calculation using the obtained mathematical model of the PA signal, Eq. (4.16), for the backward and forward propagation mode respectively. As observed experimentally, and correcting the obtained through the pressure model without considering the sensor and oscilloscope, the first peak is now bipolar due to the amplitude differences, $P_X(\tau_X - t_d) - P_X(\tau_X)$ in Eq. (4.16), generated by the sensor. These peaks do not interfere, because their width is narrow, and then the negative peak is bigger than the experimental one. The width of the experimental peaks is explained by the difference of the acoustical signals due to the sensor, despite the width of the theoretical peaks is not well defined and has a different and more complex structure, This can be explained as an effect of the acoustic wave reflections inside the sensor material and the heat diffusion from the sample to the fluid that is not considered in the mathematical model but can be implemented in future work.

(a) Electrical signals   (b) Numerical calculation
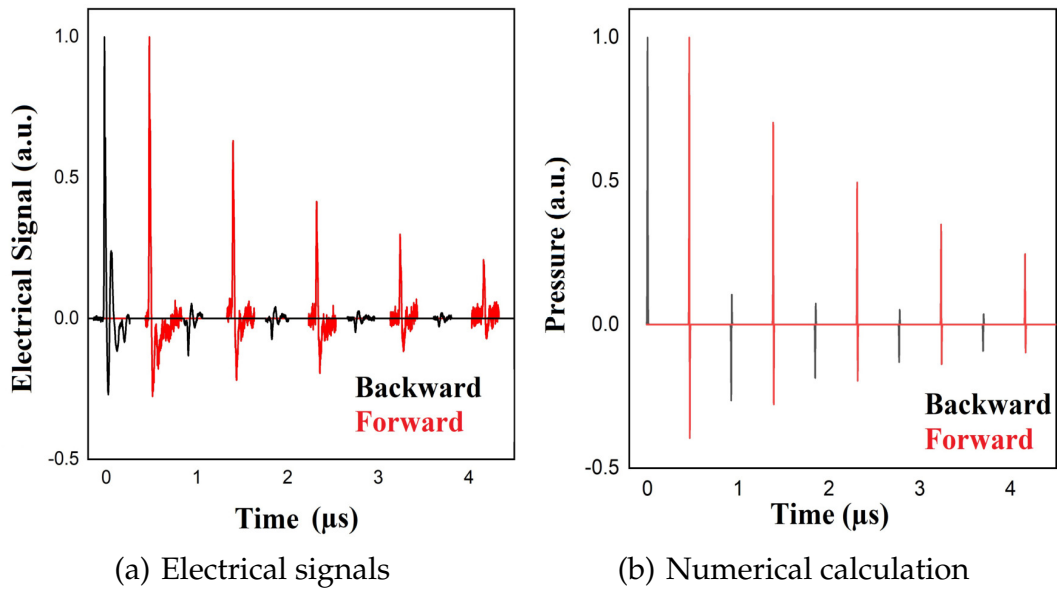
Figure 4.4: Electrical signals and the resulted numerical calculation using the Eqs. (4.9) for the backward (black) and forward (red) propagation mode.

(a) Backward   (b) Forward

Figure 4.5: Comparison between the (a) backward and (b) forward acquired electrical signals and its corresponding numerical calculation using the electrical signal model of the Eqs. (4.16). In the insets, the first peak of the experimental and the numerical result are displayed.

Chapter 5

Conclusions and perspectives

The PA imaging technique is an emerging inspection tool with potential applications in the non-invasive biomedical diagnosis, and it has been demonstrated the importance of the reconstruction algorithms for specific measurements techni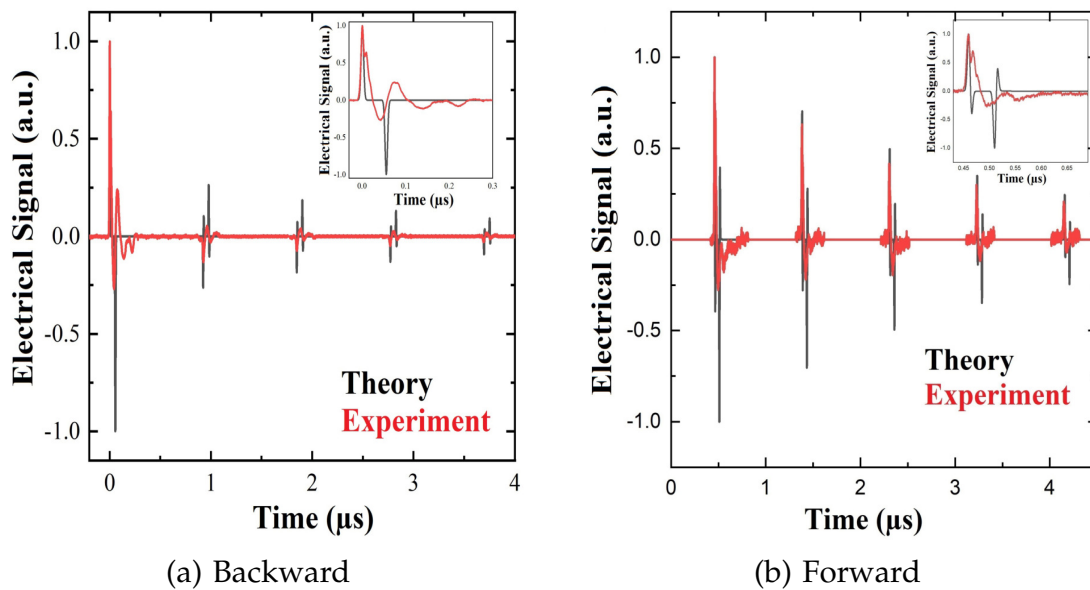ques and detection geometries. Even though the TR is a physically and mathematically robust method, when the experimental configuration does not satisfies the physical assumptions made in its formulation, the TR algorithm provides images that could lead to a wrong interpretation. On the other side, the DAS-SAFT algorithm, which make no physical assumptions moreover than a constant sound speed, will provide images with high levels of artifacts if the detection geometry is not accurately implemented during the experiments.

The SSC-SAFT is proposed in this work as a PA image reconstruction method for a single-element measurement technique and implemented considering a circular geometry of detection, considering the size of the effective area of detection of the sensor and with the physical assumption of a constant sound speed.

The single-element measurement technique avoids the need for multiple characterized sensors and the multiplexing in the data acquisition and, although this measurement technique is not practical for *in vivo* scanning, it results in a low-cost system to study and propose solutions to the PA imaging challenges. Moreover, single-element scan is the basis of PA microscopy, which makes the SSC-SAFT with potential applications in this relevant area.

By comparing the SSC-SAFT with the TR and DAS-SAFT algorithms of reconstruction, it was demonstrated that the SSC-SAFT improves, qualitatively and quantitatively, the image quality. The acoustical particle example is a proof of concept of the method, idealizing a simple and symmetrical situation but with a sparse sample, to show how the SSC-SAFT can avoid the side-lobe artifact formation. With the separate copper wires, it was shown that the SSC-SAFT can preserve a proper value of the FWHM in the image favoring the definition and spatial

resolution of the reconstructed objects. The contiguous copper wires study shows that the proposed reconstruction method improves the definition of the objects in the image by avoiding the superposition of side-lobe artifacts. Finally, the PLA decagrammic prism, shows the advantages obtained by considering the size of the effective region of detection of the sensor, reducing the artifact formation due to off-axis signals and recovering targets in the image that generates a low electrical SNR during the experiment.

The *ex-vivo* tissue study demonstrates the capabilities of the SSC-SAFT in biomedical imaging, and how its qualitatively and quantitatively improvements favor a correct interpretation of the objects recovered in the PA image, allowing the study of the PA signals of this kind of samples and to explore the medical capabilities of the PA imaging techniques. Furthermore, the SSC-SAFT has a faster performance, reducing in a 90% and 98% the time required to perform the TR and DAS-SAFT algorithms respectively.

The SSC-SAFT is presented for a circular geometry of detection because of its application on biomedical imaging through the tomographic inspection, the method can be implemented for an arbitrary geometry of detection characterizing the Cartesian coordinates of the path covered by the sensor to calculate the time delays. The SSC-SAFT considers the sensor as formed by a set of points (pixels in the image) that acquires the same signal, which is a rough approximation, further work on the mathematical modeling of the sensor detection process can be implemented in the SSC-SAFT.

Being a DAS-SAFT based image reconstruction algorithm, the SSC-SAFT is independent of the PA wave equation and of any of its assumptions, then, at its present, the SSC-SAFT does not provide any relation between the pixels intensity values of the reconstructed image and some physical parameters of the sample. Nevertheless, the waveform of the PA electrical signal can be inherited in a reconstruction line during the image formation in the SSC-SAFT. In this work, a 1-dimensional mathematical model for the PA electrical signal was presented, and it was shown that the proposed thermal correction for the PA source makes the 1-dimensional PA wave equation a proper approximation for the generation and propagation of the PA wave in solid samples with a strong optical absorption coefficient, and not only for fluids, as the PA wave equation model states.

It was proposed that the PA source is the region where the optical absorption occurs along with the region where the temperature was increased. To model the PA electrical signal using the solution proposed, the effect of the sensor and oscilloscope were modeled as a parallel RC electrical circuit, resulting in a predicted electrical signal proportional to the difference of the solutions at the faces of the

sensor. The electrical signal model was compared with the PA electrical signals generated by an aluminum slab, finding relevant information of the physical parameters carried out by the signal, and a proper match in the shape of the acquired electrical signal and the theoretical prediction. Then, the mathematical solution proposed may be implemented to characterize the wave form of the PA electrical signal generated by strong optical absorbers.

The mathematical model proposed along with the SSC-SAFT could be implemented to approach the quantitative PA imaging challenges. Since the waveform of the electrical signal is inherited in its corresponding reconstruction line during the SSC-SAFT image formation, the lateral variation profile will match, beyond a proportionality factor, the shape of this electrical signal. Then, the mathematical model could be implemented to study the characteristics and parameters of the electrical signal related to a physical parameter of the sample. These parameters of the signal, which could be its FWHM, peak-to-peak amplitude, or its exponential decay, can be correlated with those of the lateral variation profile, to find a relation between a physical parameter of the imaged sample and the intensity variation of the reconstruction line in the SSC-SAFT image. This proposal needs an extensive study of the electrical signal parameters that can be predicted with the mathematical model proposed, and, in my view, a high acquisition frequency that allows to define large numbers of nodes in the computational grid to obtain an adequate resolution in the lateral variation profiles. These hypothetical results could be of significant advance in the quantitative PA imaging being a proposition of future work related to the results and proposals of this thesis.

Bibliography

[1] Brian J. Thompson and Lihong V. Wang. *Photoacoustic Imaging and Spectroscopy*. CRC Press, 2009.

[2] Srirang Manohar and Daniel Razansky. *Adv. Opt. Photon.*, 8(4):586–617, Photoacoustics: a historical review.

[3] Paul Beard. Biomedical photoacoustic imaging. *Interface focus*, 1(4):602–31, 2011.

[4] Sarah Wilkinson, James Cummings, Sakif Zafar, Martin Kozar, Joanne Manning, Graham Dinsdale, Michael Berks, Christopher Taylor, Mark Dickinson, Ariane L Herrick, and Andrea K Murray. Photoacoustic imaging is a novel tool to measure finger artery structure and oxygenation in patients with systemic sclerosis. *Scientific Reports*, 12(1):20446, 2022.

[5] Yizhi Liang, Wubing Fu, Qiang Li, Xiaolong Chen, Huojiao Sun, Lidai Wang, Long Jin, Wei Huang, and Bai-Ou Guan. Optical-resolution functional gastrointestinal photoacoustic endoscopy based on optical heterodyne detection of ultrasound. *Nature Communications*, 13(1):7604, 2022.

[6] C Lee, M Jeon, and C Kim. 3d - photoacoustic imaging in nanomedicine. *Applications of Nanoscience in Photomedicine*, pages 31–47, 2015.

[7] Xueding Wang, Yongjiang Pang, Geng Ku, Xueyi Xie, George Stoica, and Lihong V Wang. Noninvasive laser-induced photoacoustic tomography for structural and functional in vivo imaging of the brain. *Nature Biotechnology*, 21(7):803–806, 2003.

[8] Zhen Yuan and Huabei Jiang. Quantitative photoacoustic tomography. *Philosophical transactions. Series A, Mathematical, physical, and engineering sciences*, 367(1900):3043–54, 2009.

[9] Ben Cox, Jan G Laufer, Simon R Arridge, and Paul C Beard. Quantitative spectroscopic photoacoustic imaging: a review. *Biomedical Optics*, 17(6):061202, 2012.

[10] Mithun Kuniyil Ajith Singh, Naoto Sato, Fumiyuki Ichihashi, and Yoshiyuki Sankai. *Clinical Translation of Photoacoustic Imaging - Opportunities and Challenges from an Industry Perspective*. Springer Singapore, 2020.

[11] Jimmy L Su, Bo Wang, Katheryne E Wilson, Carolyn L Bayer, Yun-Sheng Chen, Seungsoo Kim, Kimberly A Homan, and Stanislav Y Emelianov. Advances in clinical and biomedical applications of photoacoustic imaging. *Expert Opinion on Medical Diagnostics*, 4(6):497–510, 2010.

[12] Guenther Paltauf, Petra Hartmair, Georgi Kovachev, and Robert Nuster. Piezoelectric line detector array for photoacoustic tomography. *Photoacoustics*, 8, 2017.

[13] Hao Li, Biqin Dong, Zhen Zhang, Hao F Zhang, and Cheng Sun. A transparent broadband ultrasonic detector based on an optical micro-ring resonator for photoacoustic microscopy. *Scientific Reports*, 4(1):2045–2322, 2014.

[14] Warbal Pankaj and Saha Ratan. In silico evaluation of the effect of sensor directivity on photoacoustic tomography imaging. *Optik*, 252:168305, 2022.

[15] Josy John Mary and Barhumi Imad. Fast and efficient pat image reconstruction algorithms: A comparative performance analysis. *Signal Processing*, 201:108691, 2022.

[16] Eliel Hojman, Thomas Chaigne, Oren Solomon, Sylvain Gigan, Emmanuel Bossy, Yonina Eldar, and Ori Katz. Photoacoustic imaging beyond the acoustic diffraction-limit with dynamic speckle illumination and sparse joint support recovery. *Optics Express*, 25, 2016.

[17] Benjamin Cox and Bradley Treeby. Artifact trapping during time reversal photoacoustic imaging for acoustically heterogeneous media. *IEEE Transactions on Medical Imaging*, 29(2):387–396, 2010.

[18] Kang Shen, Songde Liu, Ting Feng, Jie Yuan, Benpeng Zhu, and Chao Tian. Negativity artifacts in back-projection based photoacoustic tomography. *Journal of Physics D: Applied Physics*, 54, 2020.

[19] Sandeep Kumar Kalva, Zhe Zhi Hui, and Manojit Pramanik. Calibrating reconstruction radius in a multi single-element ultrasound-transducer-based photoacoustic computed tomography system. *J. Opt. Soc. Am. A*, 35(5):764–771, 2018.

[20] Minghua Xu and Lihong Wang. Universal back-projection algorithm for photoacoustic computed tomography. *Physical review. E, Statistical, nonlinear, and soft matter physics*, 71:016706, 02 2005.

[21] Leonid A. Kunyansky. A series solution and a fast algorithm for the inversion of the spherical mean radon transform. *Inverse Problems*, 23, 2007.

[22] Yulia Hristova, Peter Kuchment, and Linh Nguyen. Reconstruction and time reversal in thermoacoustic tomography in acoustically homogeneous and inhomogeneous media. *Inverse Problems*, 24, 10 2008.

[23] R.I. Siphanto, K.K. Thumma, R.G.M. Kolkman, T.G. van Leeuwen, F.F.M. de Mul, J.W. van Neck, L.N.A. van Adrichem, and W. Steenbergen. Serial noninvasive photoacoustic imaging of neovascularization in tumor angiogenesis. *Opt. Express*, 13(1):89–95, 2005.

[24] Keerthi S. Valluru and Juergen K. Willmann. Clinical photoacoustic imaging of cancer. *Ultrasonography*, 35(4):267–280, 2016.

[25] Haeni Lee, Seongyi Han, Sinyoung Park, Seonghee Cho, Jinwoo Yoo, Chulhong Kim, and Jeesu Kim. Ultrasound-guided breath-compensation in single-element photoacoustic imaging for three-dimensional whole-body images of mice. *Frontiers in Physics*, 10, 2022.

[26] Yuning Guo, Baowen Li, and Xiaobo Yin. Single-shot compressed photoacoustic tomographic imaging with a single detector in a scattering medium. *Phys. Rev. Applied*, 13(4):044009, 2020.

[27] Lian Xiong, Jennifer M. Ruddock, and Gerald J. Diebold. Photoacoustic transients generated by laser irradiation of thin films. *Photoacoustics*, 3(2):60–63, 2015.

[28] Minghua Xu and Lihong V. Wang. Photoacoustic imaging in biomedicine. *Review of Scientific Instruments*, 77(4):041101, 2006.

[29] David Finch and Sarah K. Patch. Determining a function from its mean values over a family of spheres. *SIAM Journal on Mathematical Analysis*, 35(5):1213–1240, 2004.

[30] Bradley Treeby, Ben Cox, and Jiri Jaros. *k-Wave user manual: a Matlab toolbox for the time domain simulation of acoustic wave fields*. 2016.

[31] P. Morse and K. Ingard. *Theoretical Acoustics*. Princeton University Press, 1968.

[32] Makoto Tabei, T. Douglas Mast, and Robert C. Waag. A k-space method for coupled first-order acoustic propagation equations. *The Journal of the Acoustical Society of America*, 111(1):53–63, 2002.

[33] B. T. Cox, S. Kara, S. R. Arridge, and P. C. Beard. k-space propagation models for acoustically heterogeneous media: Application to biomedical photoacoustics. *The Journal of the Acoustical Society of America*, 121(6):3453–3464, 2007.

[34] Bradley Treeby and Ben Cox. k-wave: Matlab toolbox for the simulation and reconstruction of photoacoustic wave fields. *Biomedical Optics*, 15:021314, 03 2010.

[35] Bo Wang, Su Tianning, Pang Weiran, Wei Ningning, Xiao Jiaying, and Peng Kuan. Back-projection algorithm in generalized form for circular-scanning-based photoacoustic tomography with improved tangential resolution. *Quantitative Imaging in Medicine and Surgery*, 9(3), 2019.

[36] R. A. Brooks and G Di Chiro. Theory of image reconstruction in computed tomography. *Radiology*, 121(117):561–72, 1975.

[37] Jonathan M. Blackledge. *Digital Image Processing. Mathematical and Computational Methods*. Woodhead Publishing Series in Electronic and Optical Materials, 2006.

[38] R. Acharya, Richard M. Wasserman, John Stevens, and Carlos Hinojosa. Biomedical imaging modalities: a tutorial. *Computerized medical imaging and graphics : the official journal of the Computerized Medical Imaging Society*, 19(1):3–25, 1995.

[39] Suhyun Park, Andrei B. Karpiouk, Salavat R. Aglyamov, and Stanislav Y. Emelianov. Adaptive beamforming for photoacoustic imaging. *Opt. Lett.*, 33(12):1291–1293, 2008.

[40] Jiaying Xiao, Xiaofei Luo, Kuan Peng, and Bo Wang. Improved back-projection method for circular-scanning-based photoacoustic tomography with improved tangential resolution. *Appl. Opt.*, 56(32):8983–8990, 2017.

[41] R. A. Kruger, D. R. Reinecke, and G. A. Kruger. Thermoacoustic computed tomography - technical considerations. *Medical physics*, 26(9):1832–7, 1999.

[42] Adam Petschke and Patrick J. La Riviére. Comparison of photoacoustic image reconstruction algorithms using the channelized hotelling observer. *Biomedical Optics*, 18:026009, 2013.

[43] R C Fairchild, B H Anderson, and J R Frederick. Synthetic aperture ultrasonic inspection of pressure vessels and piping. *ASME Pressure Vessels and Piping Division*, pages 77–PVP–23, 1997.

[44] Lester W Schmerr Jr. *Fundamentals of ultrasonic phased arrays*. Springer, UK, 2015.

[45] Moein Mozaffarzadeh, Ali Mahloojifar, Mahdi Orooji, Saba Adabi, and Mohammadreza Nasiriavanaki. Double stage delay multiply and sum beamforming algorithm: Application to linear-array photoacoustic imaging. *IEEE transactions on biomedical engineering*, 65:31–42, 04 2017.

[46] H B Lim, N T Nhung, and N D Thang. Confocal microwave imaging for breast cancer detection: delay-multiply-and-sum image reconstruction algorithm. *IEEE transactions on biomedical engineering*, 55:1697–1704, 06 2008.

[47] Jeon Seungwan, Park Eun-Yeong, Choi Wonseok, Managuli Ravi, Lee Ki jong, and Kim Chulhong. Real-time delay-multiply-and-sum beamforming with coherence factor for in vivo clinical photoacoustic imaging of humans. *Photoacoustics*, 15:100136, 2019.

[48] Rafael Pérez-Solano, Francisco I. Ramirez-Perez, Jorge A. Castorena-Gonzalez, Edgar Alvarado Anell, Gerardo Gutiérrez-Juárez, and Luis Polo-Parada. An experimental and theoretical approach to the study of the photoacoustic signal produced by cancer cells. *AIP Advances*, 2(1):011102, 2012.

[49] Jorge Enrique Alba-Rosales, Gabriel Ramos-Ortiz, Lenin Francisco Escamilla-Herrera, Bartolome Reyes-Ramírez, Luis Polo-Parada, and Gerardo Gutiérrez-Juárez. Effects of optical attenuation, heat diffusion, and acoustic coherence in photoacoustic signals produced by nanoparticles. *Applied Physics Letters*, 112(14):143101, 2018.

[50] Markus W. Sigrist and Fritz K. Kneubühl. Lasergenerated stress waves in liquids. *The Journal of the Acoustical Society of America*, 64(6):1652–1663, 1978.

[51] Herrerías-Azcúe Francisco, Gonzáles Vega Arturo, Torres-Arenas José, and Gutiérrez-Juárez Gerardo. Solution for the photoacoustic wave equation with a single spatial degree of freedom, beer's law absorption of radiation and mechanical barriers. *Modern Physics Letters B*, 27(18):1350135, 2013.

[52] H. Schoeffmann, H. SchmidtKloiber, and E. Reichel. Timeresolved investigations of laserinduced shock waves in water by use of polyvinylidenefluoride hydrophones. *Journal of Applied Physics*, 63:46–51, 1988.

[53] Carlos A. Bravo-Miranda, Arturo González-Vega, and Gerardo Gutiérrez-Juárez. Influence of the size, geometry and temporal response of the finite piezoelectric sensor on the photoacoustic signal: the case of the point-like source. *Applied Physics B*, 115(4):471–482, 2014.

Dr. David Y. Delepine
Director de la División de Ciencias e Ingenierías.
Presente

Por este conducto expreso que he leído el trabajo "**Novel reconstruction algorithm for photoacoustic imaging: toward the quantitative imaging**" que para obtener el grado de Doctor en Física somete el M.F. Guadalupe Misael Ruiz Veloz. El trabajo es original, de alta calidad y tiene publicaciones derivadas de su labor de investigación, motivo por el cual expreso que el dicho trabajo cumple sobradamente con los requisitos para la obtención del grado.

Atentamente

Dr. José Luis Lucio Martínez
Departamento de Física.

DR. DAVID YVES GHISLAIN DELEPINE
DIRECTOR DE LA DIVISIÓN DE CIENCIAS E INGENIERÍAS
CAMPUS LEÓN
PRESENTE

Estimado Dr. Delepine:

Sirva la presente para hacer de su conocimiento que he revisado el trabajo titulado **"Novel reconstruction algorithm for photoacoustic imaging: toward the quantiative imaging"** que para obtener el grado de Doctor en Física pone a consideración el **M en F. Guadalupe Misael Ruiz Veloz.**

Le comunico que en mi opinión el trabajo reúne las características de nivel y calidad necesarias para una tesis de doctorado. Asimismo, he discutido con el **M. en F. Ruiz,** algunos aspectos de su trabajo y le he indicado las correcciones que considero pertinentes, las cuales ha incluido en la versión final del trabajo. De esta manera no tengo objeciones para la presentación del mismo de acuerdo a la reglamentación respectiva.

Agradeciendo la atención prestada a la presente, me despido

A T E N T A M E N T E.
"LA VERDAD OS HARÁ LIBRES"

Dr. Arturo González Vega
Profesor del DIQEB

C.c.p Guadalupe Misael Ruiz Veloz
C.c.p. Archivo AGV.

DEPARTAMENTO DE INGENIERÍAS QUÍMICA, ELECTRÓNICA Y BIOMÉDICA
Lomas del Bosque #103,
Lomas de Campestre, León Gto.
C.P. 37150
(477) 788 5100 Ext. 8435, Fax. Ext. 8410
www.diqeb.ugto.mx
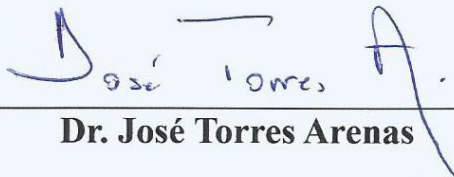
León, Guanajuato, 28 de Febrero de 2023.

Dr. David Y. Delepine
Director
División de Ciencias e Ingenierías,CLE
P R E S E N T E

Por este conducto me permito comunicarle que, en relación a la tesis: **"Novel reconstruction algorithm for photoacoustic imaging:toward the quatitative imaging"**, que presenta el Maestro en Física **Guadalupe Misael Ruiz Veloz** para obtener el grado de Doctor en Física, he leído detenidamente el documento, aportando sugerencias, correcciones, y discutido ampliamente su contenido con el alumno.

Después de lo anterior expreso mi conformidad con su contenido considerando el trabajo de un nivel adecuado como trabajo de doctorado, no teniendo inconveniente en que el mencionado trabajo sea defendido por el interesado cuando a él convenga.

Sin otro particular, aprovecho la presente para enviarle cordiales saludos.

ATENTAMENTE
"LA VERDAD OS HARÁ LIBRES"

Dr. José Torres Arenas

Dr. David Delepine
Director de la División de Ciencias e Ingenierías, Campus León
UNIVERSIDAD DE GUANAJUATO
P R E S E N T E

Por medio de la presente en mi carácter de revisor del trabajo de tesis titulado: ***"Novel reconstruction algorithm for photoacoustic imaging: toward the quantitative imaging."*** para obtener el título de **Doctor en Física** que presenta **Misael Ruiz veloz**.

Me permito comunicarle que he leído y discutido dicho trabajo con él, tengo conocimiento de todas sus contribuciones científicas, y considero que por esto, reúne los requisitos y méritos suficientes para poder continuar con sus trámites de solicitud de examen de grado y ser presentado.

Sin otro particular por el momento, aprovecho para reiterarle las seguridades de mi consideración más distinguida.

Atentamente

Rigoberto Castro B.

Dr. Rigoberto Castro Beltrán
Profesor Investigador
Departamento de Ingeniería Física

León, Gto., a 24 de febrero de 2023
Asunto: **Revisión de Tesis**

DR. DAVID YVES GHISLAIN DELEPINE
DIRECTOR
DIVISIÓN DE CIENCIAS E INGENIERIAS
CL -UNIVERSIDAD DE GUANAJUATO

A través de la presente constato que he revisado la tesis del C. M. F. **Guadalupe Misael Ruiz Veloz** con el fin de obtener el grado de Doctorado en Física. Su trabajo de tesis se titula **"Novel reconstruction algorithm for photoacoustic imaging: toward the quantitative imaging"**. En su trabajo de investigación, Misael desarrolla metodologías de reconstrucción de contornos de objetos en 3D usando señales fotoacústicas y algoritmos de reconstrucción inversa. El trabajo demuestra el potencial de las técnicas desarrolladas por Misael, las cuales son muy novedosas en su campo. El trabajo de titulación satisface con la completez y solidez de un proyecto de titulación a nivel doctorad. Misael ha realizado las correcciones recomendadas al documento de la tesis. Además, Misael ha respondido satisfactoriamente preguntes sobre los temas relacionados a su trabajo de tesis, demostrando su dominio en los temas abordados en su trabajo de tesis. Por lo que considero que ya puede proceder con los trámites para la disertación de tesis.

Sin más por el momento le envío saludos cordiales.

Atentamente

Dr. Carlos Herman Wiechers Medina
Profesor-Investigador

Tel. +52 (477) 7885100 Ext. 8467
Cel. +52 (477) 1080605
e-mail 1: carherwm@fisica.ugto.mx
e-mail 2: ch.wiechers@ugto.mx

División de Ciencias e Ingenierías
Loma del Bosque # 103, Col. Loma del Campestre. León, Guanajuato, México. C. P. 37150
Tel: +52 (477) 7885100 Exts. 8420 y 8421, Fax. Ext. 8410. www.dci.ugto.mx

**CENTRO DE INVESTIGACIONES
EN OPTICA, A.C.**

León, Guanajuato; febrero 23, 2023

ASUNTO: Aprobación de Documento de Tesis

Dr. David Yves Ghislain Delepine
Director de la División de Ciencias e Ingenierías
Campus León
Universidad de Guanajuato

Presente.

Apreciable Dr. Delepine.

A través de este medio me dirijo a usted para informarle que, a petición de los interesados, he leído el documento titulado "*Novel reconstruction algorithm for photoacoustic imaging: toward the quantitative imaging*", cuyo autor es el **M. F. Guadalupe Misael Ruiz Veloz**. El contenido ha sido discutido con el M. F. Ruiz y su asesor, Dr. Gerardo Gutiérrez Juárez, quienes han tenido a bien incluir algunas de las sugerencias de cambio planteadas por un servidor y argumentar convincentemente aquellas que fueron descartadas. Por lo anterior, considero que el trabajo de Tesis que presenta el interesado para obtener el grado de *Doctor en Física* cumple con los requerimientos que la Universidad de Guanajuato establece para proceder a su defensa en un examen recepcional.

Sin más por el momento, agradezco su atención y quedo atento para ampliar, en caso necesario, la información que considere pertinente al asunto en cuestión.

Atentamente,

Dr. Geminiano Martínez Ponce
Investigador
Centro de Investigaciones en Óptica, A. C.
Tel.: (+52) 477 4414200 Ext. 285
Correo-e: geminis@cio.mx

SALUD
SECRETARÍA DE SALUD

HOSPITAL
GENERAL
de MÉXICO
DR. EDUARDO LICEAGA

27 febrero del 2023, CDMX.

ASUNTO: Carta aceptación de tesis

A quien corresponda,

Por este medio hago saber que he leído, revisado y hecho las observaciones al trabajo de tesis que, bajo el título: "Novel reconstruction algorithm for photoacoustic imaging: toward the quantitative imaging", defenderá el C. Guadalupe Misael Ruiz Veloz, estudiante de Doctorado en Física de la Universidad de Guanajuato.

Misael Ruiz ha realizado los cambios sugeridos a su trabajo de tesis por lo que considero que su trabajo es aceptable y está listo para ser defendido.

Agradeciendo la atención a la presente.

Dra. Argelia Pérez Pacheco
Unidad de Investigación y Desarrollo Tecnológico (UIDT)
Hospital General de México Dr. Eduardo Liceaga
tel. 55 27892000 ext. 1242 y 1853
e-mail: argeliapp@ciencias.unam.mx

DIRECCIÓN DE INVESTIGACIÓN
Dr. Balmis 148, Doctores, Cuauhtémoc, 06720 Ciudad de México, CDMX
Tel: (55) 2789 2000 eXT. 5658,5656 www.hgm.saludgob.mx

UIDT
CCADET-HGM
UNIDAD DE INVESTIGACIÓN Y DESARROLLO TECNOLÓGICO

2023
AÑO DE
Francisco
VILLA
EL REVOLUCIONARIO DEL PUEBLO